International Journal of Plasticity 125 (2020) 294–313

Contents lists available at ScienceDirect

International Journal of Plasticity

journal homepage: http://www.elsevier.com/locate/ijplas

Polycrystal plasticity modeling for load reversals in commercially pure titanium

Jiaxiang Wang [a,*], Milovan Zecevic [b], Marko Knezevic [b], Irene J. Beyerlein [c]

[a] Department of Mechanical Engineering, University of California at Santa Barbara, Santa Barbara, CA, 93106, USA
[b] Department of Mechanical Engineering, University of New Hampshire, Durham, NH, 03824, USA
[c] Department of Mechanical Engineering, Materials Department, University of California at Santa Barbara, Santa Barbara, CA, 93106, USA

ARTICLE INFO

Keywords:
Backstress
Elastic-viscoplastic material
Twinning
Dislocations
Crystal plasticity

ABSTRACT

In this work, we use polycrystal modeling to study the interactions between slip and twinning during load reversals of commercially pure titanium. The constitutive response incorporates anisotropic elasticity, crystal plasticity, a dislocation density based hardening law for prismatic slip, basal slip, and pyramidal type I $\langle c+a\rangle$ slip, and micromechanical model for twin reorientation on two types: $\{10\bar{1}2\}$ extension twinning and $\{11\bar{2}2\}$ contraction twinning. The key feature of the model is the inclusion of slip-system level backstress development due to dislocation density accumulation. To demonstrate, the model is used to simulate the stress-strain response and texture evolution in a series of compression-tension and tension-compression tests carried out to different strain levels and applied in two different load directions to a strongly textured CP-Ti plate. Material parameters associated with the slip strengths for the three slip modes are reported. The model identifies the few systems within the pyramidal $\langle c+a\rangle$ slip mode as developing the most backstress among the three slip modes. It also indicates that the backstresses that develop in the forward loading path promote pyramidal slip in the reversal loading path. We also find that reverse loading changes negligibly the relative slip mode contributions from monotonic loading but it strongly affects the twinning-detwinning behavior. This work highlights the ability of polycrystal modeling to account for the co-dependent nature of multiple crystallographic slip and twinning modes, the hysteresis in plastic response during the forward-reversal cycle, and the two sources of hardening engendered by history-dependent dislocation density accumulation.

1. Introduction

Titanium and its alloys are used in many applications that require the material to undergo cyclic loading (Hama et al., 2015; Benmhenni et al., 2013). Like many metals with a low symmetry, hexagonal close packed (HCP) crystal structure, the plastic response of Ti is governed by the formation and propagation of two defect-driven mechanisms, slip and twinning (Won et al., 2015, 2017; Hosford, 1993; Warwick et al., 2012; Chichili et al., 1998; Becker and Pantleon, 2013; Hama et al., 2012). Further, there are many modes by which slip and twinning have been observed to use. For commercially pure titanium (CP-Ti) in ambient conditions, for instance, slip can occur via prismatic $\langle a\rangle$ slip, pyramidal $\langle c+a\rangle$ slip, and basal $\langle a\rangle$ slip (Benmhenni et al., 2013; Warwick et al., 2012;

* Corresponding author.
E-mail address: jiaxiangwang@ucsb.edu (J. Wang).

https://doi.org/10.1016/j.ijplas.2019.09.013
Received 27 May 2019; Received in revised form 22 September 2019; Accepted 23 September 2019
Available online 4 October 2019

Becker and Pantleon, 2013; Hama et al., 2015). At the same time, Ti can also exhibit a large amount of twinning via $\{10\bar{1}2\}$ extension twinning, as well as $\{11\bar{2}2\}$ contraction twinning (Hama et al., 2015; Mullins and Patchett, 1981; Conrad, 1981). The number and kind of slip and twinning modes that actually operate during deformation depend on the load/material orientation relationship and the loading temperature and strain rate (Paton and Backofen, 1970; Hama et al., 2015). This multiplicity in deformation mechanisms renders the macroscopic deformation response of Ti highly anisotropic, and much more temperature and rate sensitive than metals with simpler crystal structures, like body-centered cubic (BCC) and face-centered cubic (FCC).

It is important for shaping and designing parts made from commercially pure (CP-)Ti and Ti alloys that the relationship between the mechanisms, microstructure, and plastic response are quantifiable and predictable. The origins of plastic anisotropy can be traced to a combination of the strong anisotropy among the slip and twin modes of the HCP structure and strong initial texture typical of processed HCP metals. Studies employing crystal plasticity based models can consider both elements in the calculation and have demonstrated success in predicting plastic anisotropic of Ti under monotonic loading (Yapici et al., 2006; Suwas et al., 2011; Gurao et al., 2011; Gloaguen et al., 2013; Knezevic et al., 2013; Hama et al., 2016; Sinha et al., 2016; Wronski et al., 2018). The crystal-plasticity finite-element method was used by Hama et al. (2016) to examine the deformation mechanism in a CP-Ti sheet during monotonic loading process. A Taylor-type crystal plasticity model was used to predict the crystallographic texture evolution and anisotropic stress-strain response of these materials during large plastic strains at ambient temperature (Wu et al., 2008). In all these cases it is found that the values set for the individual slip and twin strengths of each mode and the initial texture of the sample dictate the relative amounts of slip and twinning, which in turn, greatly affect the predicted flow stress and hardening rate. Comparatively, however, modeling the behavior of CP-Ti and other Ti alloys in strain path changes has not received as much attention, despite the fact that cyclic conditions are frequently encountered in structural applications.

Cyclic loading involves a forward-reverse strain path change, wherein the first deformation path is followed by second deformation path in the opposite direction. In cyclic loading, a phenomenon called the Bauschinger effect (BE) (Bauschinger, 1886) is commonly observed in both single crystals and polycrystals (Nieh and Nix, 1986; Sauzay, 2008; Buckley and Entwistle, 1956; Demir and Raabe, 2010). The BE refers to a reduction in the yield stress and change of work hardening rate in the reverse path compared to those in the forward path (Hasegawa et al., 1975; Kitayama et al., 2013; Stout and Rollett, 1990; Wilson et al., 1990; Bate and Wilson, 1986; Orowan, 1959; Zang et al., 2013). The BE is conventionally attributed to internal backstresses that develop during forward loading that resists dislocation motion. When the macroscopic applied strain subsequently reverses direction, the same backstress acts as a forward stress that can add to the driving force to move dislocations in the opposite direction. The nature of the backstress in polycrystals can be intra-granular (type III stresses) or inter-granular (type II stresses). Intra-granular stresses are typically associated with incompatibility between hard regions of high dislocation density and soft regions of low dislocation density (Hama et al., 2015; Mughrabi, 1983; Kassner et al., 2013), whereas inter-granular stresses result from differences in the elastic and plastic response between neighboring grains, manifesting as dislocation pile ups at obstacles within the grain or at grain boundaries (Zecevic and Knezevic, 2015; Weng, 1980; Weng, 1979; Seeger,1957).

A few studies have experimentally studied the cyclic behavior of CP-Ti. Shamsaei et al. (2010) and Peng et al. (2014) conducted fatigue tests on CP-Ti, focusing on the characteristics of the stress-strain response and fatigue life. Tritschler et al. (2014) performed cyclic loading tests in a Ti alloy sheet and modeled the work-hardening behavior. In these studies, the activity of twinning and its effect on the work-hardening behavior were not studied in their work. Hama et al. (2015) studied the working hardening behavior and twinning behavior in a CP-Ti under monotonic and forward-reversal loading. In the former case, they observed twinning and tension-compression asymmetry in the work-hardening but not in the yield stress. Regarding the latter load reversal response, a BE effect and detwinning upon reverse loading were observed (Hama et al., 2015). The connection between the hardening and other flow stress characteristics seen in the strain path change test with the underlying twinning or slip behavior, however, has yet to be clarified.

Crystal plasticity (CP) based polycrystal modeling has been widely used to connect macroscopic changes in plastic response as a result of a strain path change, such as cyclic loading. Among the available CP models, there are those that only consider plastic behavior, such as the visco-plastic self-consistent model (VPSC), and those that treat elastic and plastic behavior, such as the elasto-plastic self-consistent (EPSC) model and elastic viscoplastic self-consistent (EVPSC) model (Ma et al., 2019; Turner and Tomé, 1994; Lebensohn and Tomé, 1993; Wang et al., 2013a,b) In these models, a homogenous stress and strain rate for every grain in the polycrystal is calculated. Each orientation is an ellipsoid in a homogeneous effective medium (HEM) that bears the average properties of the polycrystal. The homogenized or mean-field response models, such as self-consistent models, take only a statistical description of the microstructure as input (e.g., crystallographic texture) and return a sample scale or effective response and microstructure evolution. While these models do not resolve stress or strain rate below that of a grain, the stress and strain rate of individual grains differ from that of the HEM.

In contrast to self-consistent models, crystal plasticity finite element or crystal plasticity fast Fourier transform (FFT) models (Ardeljan et al., 2015, 2016; Kalidindi et al., 2006; Knezevic et al., 2014, 2013b; Lebensohn et al., 2012; Zecevic et al., 2015) can calculate the spatially resolved mechanical fields, including intra- and inter-granular fields in 3D. Such full-field micromechanical models require as input an explicit spatially resolved description of the material structure (e.g., grain orientation map) and return the spatially resolved material response and local structural evolution. Compared to the self-consistent schemes, they are, however, more computationally intensive for simulating deformation sequences involving multiple paths in series and nucleation and growth of deformation twin lamellae.

For modeling constitutive response under strain path changes, more recent self-consistent formulations involving advanced constitutive laws have been developed. In some works (Kitayama et al., 2013; Knezevic et al., 2013a; Wen et al., 2014), VPSC was combined with a dislocation based hardening law to model the BE effect and subsequent working hardening rate upon strain reversal.

These models captured the reverse hardening rate by introducing a reversible dislocation population that accumulates in prestraining and annihilates upon strain reversal. However, these models do not account for elastic deformation and dislocation motion was not linked to the development of backstresses. Prior attempts for modeling load reversals have also involved the EPSC or EVPSC model (Lorentzen et al., 2012; Ma et al., 2019). It was shown in Lorentzen et al. (2012) that even with inter-granular backstresses (type II stresses) taken into account, the EPSC was insufficient for predicting the behavior of stainless steel under cyclic deformation. By incorporating a slip-system-level backstress evolution law for intra-granular stresses (type III stresses), the EPSC model was able to capture subsequent hardening behavior under the reverse strain path change (Zecevic and Knezevic, 2015; Zecevic and Knezevic, 2018). To date, this EPSC scheme with inter- and intra-granular stresses has been applied to model the large strain cyclic deformation of a dual phase steel DP590 (Zecevic et al., 2016) and the Inconel 718 Ni-based superalloy (Ghorbanpour et al., 2017). These studies, however, treated materials with either an FCC or BCC crystal structure. For modeling load reversal sequences in HCP materials, like Ti and Mg, the interactions of twinning and detwinning with elasticity, multiple slip modes, and type III backstress development need to also be taken into account.

In this work, we present an EPSC model that accounts for dislocation density based hardening on slip systems, inter- and intra-granular stresses backstress evolution due to slip, and subgrain reorientation due to twinning and detwinning, to understand and evaluate the mechanisms underlying the deformation response of CP-Ti in load reversals. A second goal is to elucidate the effect of type III backstress evolution on deformation twinning. The model is developed to incorporate the multiple slip modes and multiple twinning modes commonly associated with the deformation of CP-Ti. Forward-reverse stress-strain data are taken from an earlier work (Hama et al., 2015), which includes texture evolution and different loading sequences and amounts of strains. Notably, here, only one set of material parameters is characterized for all data sets. With the model, we first we demonstrate that the decrease in yield stress (i.e., BE effect) and increase in strain hardening observed during reverse loading can be linked the development of type III backstresses. The analysis also indicates that backstress levels are high when pyramidal slip is active and tend to promote the activity of deformation twinning in forward loading. We show that straining in the forward direction can hinder the activation of other twins in subsequent straining in the reverse direction.

This paper is organized as follows. We begin with a brief review of the load reversal experiments reported in (Hama et al., 2015) and the deformation mechanisms reported in prior experimental studies on CP-Ti. Next, the EPSC model is presented, including the treatments for slip-level backstress development, dislocation affected hardening, and twinning/detwinning processes. The model application and validation to the load reversal experiments is presented, including direct comparisons with stress-strain responses in all load sequences, directions, and strain levels, for the same set of parameters. Comparisons with available texture measurements are also included. We then show additional predictions not available experimentally, such as the initial slip strengths and material parameters governing dislocation storage, and discuss the active slip and twinning systems and their relative contributions to accommodating strain during loading and reloading. Last, since type III backstresses can be relatively small in magnitude compared to the overall flow stress, we take the opportunity to repeat some calculations without the backstress development in order to further discuss the interrelationship between deformation twinning and backstress development. While the EPSC model employed here intrinsically cannot provide a local description of the internal stresses in the grain boundaries, it can offer an average description of the relative amounts of each slip and twinning system as they evolve in loading and reverse loading cycle and a first look at the inter-relationships between slip, backstress development, and twinning.

2. CP-Ti slip and twinning modes

One goal of this work is to study slip and twinning activity and slip-twin interactions during a load reversal cycle. To this end, CP-Ti is an excellent choice. As mentioned in the introduction, plastic deformation of CP-Ti is accommodated by a multiplicity of slip and twinning modes. The main slip modes in CP-Ti are prismatic $\langle a\rangle$ slip, basal $\langle a\rangle$ slip, and pyramidal $\langle c+a\rangle$ slip. At room temperature, $\{10\bar{1}0\}\langle 11\bar{2}0\rangle$ is believed to be the easiest slip mode to activate. Other possible slip modes are $\{0001\}\langle 11\bar{2}0\rangle$ basal slip, and $\{10\bar{1}1\}\langle 11\bar{2}3\rangle$ pyramidal slip modes (Won et al., 2015, 2017; Hosford, 1993; Warwick et al., 2012; Chichili et al., 1998).

Several types of twins have been observed in CP-Ti: $\{10\bar{1}2\}, \{11\bar{2}1\}$ extension twins and $\{11\bar{2}2\}, \{10\bar{1}1\}, \{11\bar{2}4\}$ contraction twins. In the study by Hama et al. (2015) of CP-Ti, twin types and volume fractions were obtained via EBSD. They observed $\{10\bar{1}2\}$ twinning, $\{11\bar{2}2\}$ twinning and $\{11\bar{2}1\}$ twinning during tension in the RD. In high-strain rate conditions, Xu et al. (2012) reported the formation of $\{11\bar{2}2\}$ and $\{11\bar{2}4\}$ twins. A wire-drawn CP-Ti sample test performed by Stanford et al. (2008) observed that $\{10\bar{1}2\}$ extension twinning is the most active extension twin mode and $\{11\bar{2}2\}$ twinning an active contraction twin mode. Becker and Pantleon (2013) conducted a tensile test based on rolled CP-Ti, which aimed to identify three different work-hardening stages. They found that $\{11\bar{2}2\}$ twinning and $\{10\bar{1}2\}$ twinning were activated in the second and third stages. At room temperature, other twin modes, such as $\{11\bar{2}1\}$ extension twinning and $\{10\bar{1}1\}$ contraction twinning, are relatively difficult to activate. $\{10\bar{1}1\}$ contraction twinning, for instance, has been reported at temperatures above 300 $^{\circ}C$. Evidently, from the studies carried out to date, contraction $\{11\bar{2}2\}$ twinning (CTW) and extension $\{10\bar{1}2\}$ twinning (TTW) are common twinning modes for CP-Ti in room temperature deformation. Accordingly, we made these two twinning modes available to the calculations that follow.

3. Experimental background

Recently, Hama et al. performed experiments to investigate the work hardening and twinning behavior in a CP-Ti under large strain

cyclic loading (Hama et al., 2015). In their experiment, a cold-rolled CP-Ti sheet (Kobe Steel, JIS grade 2) with 1 mm thickness was used. The present study uses data from their experiment in order to understand the contributions of slip and twinning in the deformation of CP-Ti during cyclic loading.

In their work, samples were cut parallel to the RD direction (RD sample) and TD direction (TD sample). All samples were annealed for approximately one hour before testing. The average grain size is 20 μm. Fig. 4(a) presents the pole figures of the initial texture of the sample. Monotonic tension, compression, tension followed by compression(T-C) and compression followed by tension (C-T) were performed on the RD and TD samples. A 9 MPa through-thickness stress was applied by comb-shaped dies to prevent buckling during compression. Mineral hydraulic oil was used to reduce the friction between the die and specimen. The tests were conducted with an initial strain rate of $6.67 \times 10^{-4} s^{-1}$ (see Fig. 3).

In view of the initial texture in Fig. 4(a) of their rolled sheet, it is possible surmise which of the two types of twin modes could be activated during RD and TD cyclic tests. In-plane compression in the RD would generate a local normal tensile stress component along the c-axes in many grains while in-plane tension would generate a local normal compression component. It can, therefore, be expected that in-plane compression would be suitable for activating TTWing and in-plane tension CTWing.

These expectations are consistent with the modeling that has been performed to date. For this same initial texture, Hama et al. (2016) applied a crystal-plasticity finite-element model to study the material response under monotonic loading, either in tension or compression along the RD direction. The initial crystallographic orientations assigned to the elements were randomly selected from a result of EBSD measurement and five families of slip were made available: basal $\{0001\}\langle 11\bar{2}0\rangle$ slip, prismatic $\{10\bar{1}0\}\langle 11\bar{2}0\rangle$ slip, pyramidal $\{10\bar{1}1\}\langle 11\bar{2}0\rangle$ slip, pyramidal $\{11\bar{2}2\}\langle 11\bar{2}3\rangle$ slip, and pyramidal $\{10\bar{1}1\}\langle 11\bar{2}3\rangle$ slip, as well as two families of twinning systems: $\{10\bar{1}2\}$ twinning and $\{11\bar{2}2\}$ twinning. Their modeling results indicated that $\{11\bar{2}2\}$ twinning was activated under RD tension, while $\{10\bar{1}2\}$ twinning was activated under RD compression (Hama et al., 2016).

The properties, particularly in directionality, of these two twin types would suggest that when considering cyclic loading, the order taken in the forward-reverse cyclic loading would lead to different responses. In a forward-reverse load cycle, such as compression-tension, TTWing resulting from the pre-strain compression step would influence the behavior of slip and twinning in the subsequent tension reloading step. Similarly, for the tension-compression cycle, CTWing generated in the pre-loading tension step would affect the slip and twinning activity in the subsequent compression reloading step. However, the underlying slip or twinning mechanisms operating in the cyclic loading would not be so easily apparent in measurements of stress-strain response or EBSD alone. The objective of the modeling effort is to determine the amounts of slip and twinning in each step and whether the mechanisms operating in forward loading alter those in reverse loading.

4. Model description

4.1. Elasto-plastic self-consistent (EPSC) model

Details of EPSC are briefly reviewed in this section, following the formulation given in (Hutchinson, 1970; Turner and Tomé, 1994; Won et al., 2015). In what follows," ·" will represent a dot product," ⊗" will represent a tensor product, vector and tensors are indicated by boldfaced characters, while scalars and tensor components are italicized and not boldfaced. For a second-order tensor **A**, the notation $\mathbf{A}^T$ denotes its transpose, and the notation *tr***A** means its trace.

In EPSC, the polycrystal is represented by a set of grains. Each grain is treated as an elasto-plastic inclusion embedded in a homogeneous equivalent matrix (HEM). The mechanics of the inclusion are solved using a Green's function approach and the individual grains interact only with the HEM. Each grain, embedded in a polycrystal, has a distinct crystallographic lattice orientation and volume fraction. In EPSC, a linearized relationship is employed at the scale of the individual grain, in which the Jaumann stress rate, $\hat{\boldsymbol{\sigma}}$, and the strain rate in grain c, $\dot{\boldsymbol{\varepsilon}}^c$ are related by:

$$\hat{\boldsymbol{\sigma}}^c = \mathbf{L}^c \dot{\boldsymbol{\varepsilon}}^c \tag{1}$$

where $\mathbf{L}^c$ is the instantaneous stiffness of the grain. The macroscopic, polycrystalline Jaumann stress rate and strain rate are equal to the volume average of the Jaumann grain stress and strain rate, i.e., $\hat{\boldsymbol{\sigma}} = <\hat{\boldsymbol{\sigma}}^c>$ and $\dot{\boldsymbol{\varepsilon}} = <\dot{\boldsymbol{\varepsilon}}^c>$ and therefore, their relationship is also linear and given by.

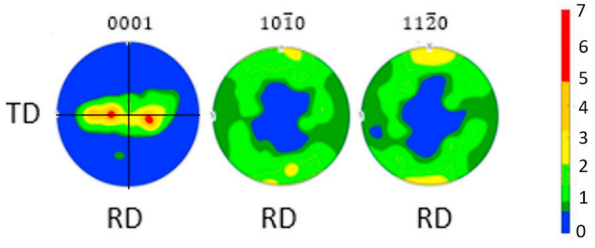

Fig. 1. Pole figures showing the initial texture of the CP-Ti material used in simulation.

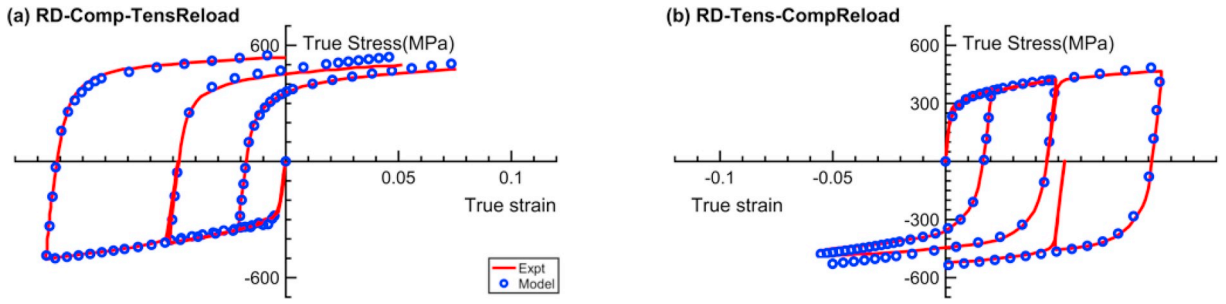

Fig. 2. Comparison of the measured and calculated true stress-true strain response of CP-Ti when deformed in the RD direction (a) Compression followed by a tension reload (CT), (b) and tension followed by a compression reload (TC). Experimental data are taken from Hama et al. (2015).

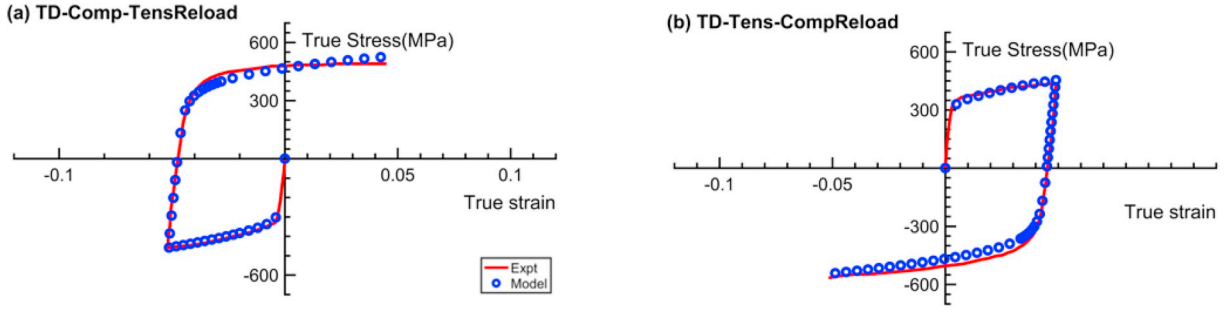

Fig. 3. Comparison of the measured and calculated true stress-true strain response of CP-Ti when deformed in the TD direction (a) CT, (b) TC. Experimental data are taken from Hama et al. (2015).

$$\widehat{\boldsymbol{\sigma}} = \mathbf{L}\dot{\boldsymbol{\varepsilon}} \tag{2}$$

where $\mathbf{L}$ is the unknown instantaneous elasto-plastic stiffness tensor of the HEM. As will be described shortly, $\mathbf{L}$ is calculated iteratively using the self-consistent procedure (Eshelby, 1957; Turner and Tomé, 1994). The macroscale Cauchy stress rate $\dot{\boldsymbol{\sigma}}$ is related to the macroscale Jaumann stress rate $\widehat{\boldsymbol{\sigma}}$ via:

$$\dot{\boldsymbol{\sigma}} = \widehat{\boldsymbol{\sigma}} + < \mathbf{W}^c\boldsymbol{\sigma}^c > - < \boldsymbol{\sigma}^c\mathbf{W}^c > = \mathbf{L}\dot{\boldsymbol{\varepsilon}} + < \mathbf{W}^c\boldsymbol{\sigma}^c > - < \boldsymbol{\sigma}^c\mathbf{W}^c > \tag{3}$$

where $\mathbf{W}^c$ is elastic spin of crystal, c. The Cauchy stress $\boldsymbol{\sigma}$ is determined by explicit integration of the Cauchy stress rate $\dot{\boldsymbol{\sigma}}$ at the end of each time increment (see Appendix).

The response of each grain c follows from solving the stress equilibrium and compatibility relations for an inclusion embedded in a homogeneous anisotropic matrix under applied loads (Turner and Tomé, 1994; Eshelby, 1957). The stress and strain rate in a grain is related to those in the macroscopic medium through the following interaction equation

$$\widehat{\boldsymbol{\sigma}}^c - \boldsymbol{\sigma} = -\mathbf{L}^{c^*}(\dot{\boldsymbol{\varepsilon}}^c - \dot{\boldsymbol{\varepsilon}}), \tag{4}$$

where $\mathbf{L}^{c^*} = \mathbf{L}(\mathbf{S}^{c^{-1}} - \mathbf{I})$ is the effective stiffness. $\mathbf{S}^c$ is the symmetric portion of Eshelby tensor and $\mathbf{I}$ is the fourth ranked identity matrix. The equation for the grain scale strain then follows as

$$\dot{\boldsymbol{\varepsilon}}^c = \mathbf{A}^c\dot{\boldsymbol{\varepsilon}} \tag{5}$$

where $\mathbf{A}^c = (\mathbf{L}^c + \mathbf{L}^{c^*})^{-1}(\mathbf{L}^{c^*} + \mathbf{L})$, and $\mathbf{L} = < \mathbf{L}^c\mathbf{A}^c >< \mathbf{A}^c >^{-1}$. From prior work by Wollmershauser et al. (2012) the driving force (resolved shear stress) for the activation of slip system is influenced by the applied loading, inter-granular stresses originating from the EPSC description of grain interaction, $\mathbf{m}^{c,s}$, and the slip system intra-granular backstress $\tau_{bs}^{c,s}$. Here $\mathbf{m}^{c,s}$ is the Schmid tensor ($\mathbf{m}^{c,s} = 0.5(\mathbf{b}^{c,s} \otimes \mathbf{n}^{c,s} + \mathbf{n}^{c,s} \otimes \mathbf{b}^{c,s})$, where $\mathbf{b}^{c,s}$ and $\mathbf{n}^{c,s}$ are the slip direction and slip plane normal.). Two conditions must be satisfied: (1) $\mathbf{m}^{c,s} \cdot \boldsymbol{\sigma}^c - \tau_{bs}^{c,s} = \tau_c^{c,s}$, meaning that the resolved shear stress reduced by the value of backstress reaches the value of slip resistance and (2) $\mathbf{m}^{c,s} \cdot \widehat{\boldsymbol{\sigma}}^c - \dot{\tau}_{bs}^{c,s} = \dot{\tau}_c^{c,s}$, meaning that the stress has to remain on the single crystal yield surface, which evolves due to hardening. The hardening matrix, $h^{ss'}$ and backstress interaction matrix, $h_{bs}^{ss'}$ are introduced to account for any coupling between the rate of slip resistance $\dot{\tau}_c^{c,s}$ and rate of backstress $\dot{\tau}_{bs}^{c,s}$, respectively, to the slip rate on other active slip systems through:

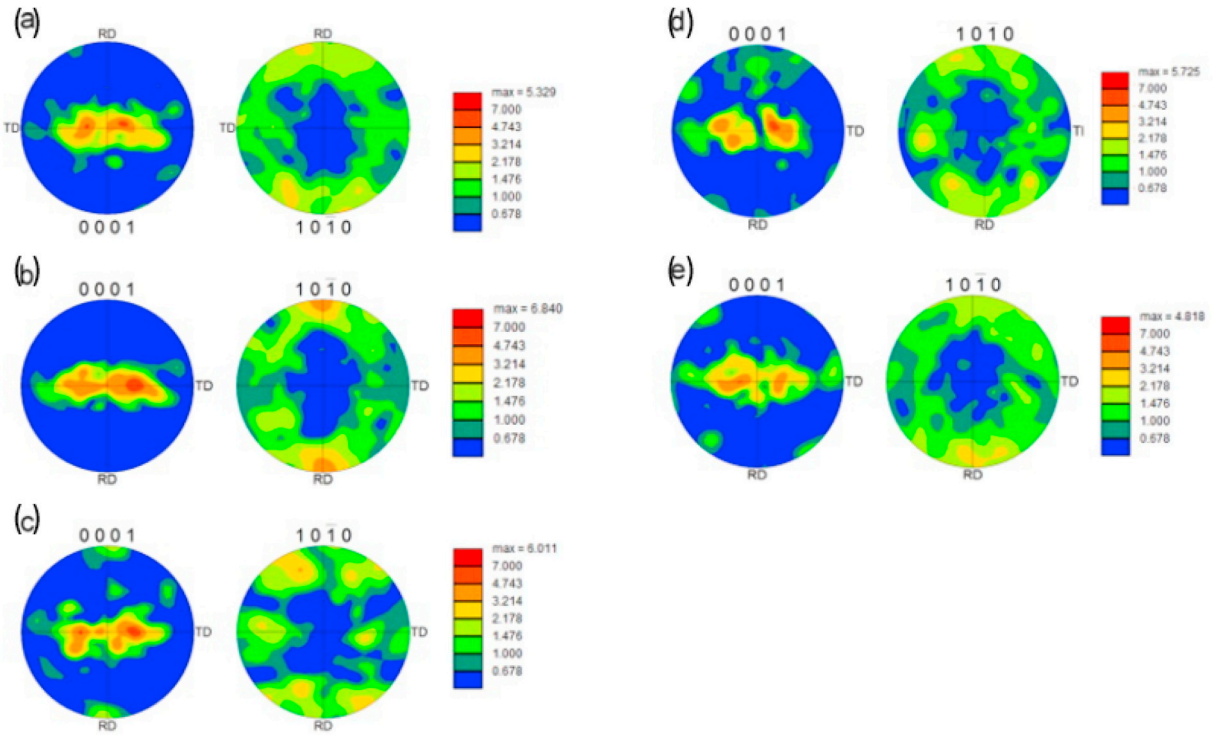

Fig. 4. Experimental results taken from Hama et al. (2015) showing the {0001} pole figures for the (a) initial texture and (b–e) samples deformed in the RD direction: (b) texture at 0.1 strain during the tension in TC loading (c) texture at −0.1 strain during compression in CT loading, (d) and (e) textures at −0.05 and 0 strain, respectively, during reverse loading in CT loading.

$$\dot{\tau}_c^{c,s} = \sum_s h^{ss'} \dot{\gamma}^{c,s'} \tag{6}$$

$$\dot{\tau}_{bs}^{c,s} = \sum_{s'} h_{bs}^{ss'} \dot{\gamma}^{c,s'} \tag{7}$$

For the individual grain c, the stress increment and strain increment also follow a constitutive relation given by

$$\widehat{\boldsymbol{\sigma}}^{\mathbf{c}} = \mathbf{C}^c(\dot{\boldsymbol{\varepsilon}}^c - \sum_s \mathbf{m}^{c,s}\dot{\gamma}^{c,s}) - \boldsymbol{\sigma}^c tr(\dot{\boldsymbol{\varepsilon}}^c) \tag{8}$$

where $\mathbf{C}^c$ is the single crystal elastic stiffness tensor and $\sum_s \mathbf{m}^{c,s}\dot{\gamma}^{c,s}$, is the plastic strain rate comprised of the slip system shear rates. From Eqs. (1), (6) and (8), $\mathbf{L}^c$ becomes:

$$\mathbf{L}^c = \mathbf{C}^c - \mathbf{C}^c \sum_s \mathbf{m}^{c,s} \otimes \left(\sum_{s'} (X^{ss'})^{-1} \mathbf{m}^{c,s'} (\mathbf{C}^c - \boldsymbol{\sigma}^c \otimes \mathbf{i})\right) - \boldsymbol{\sigma}^c \otimes \mathbf{i} \tag{9}$$

where $\mathbf{i}$ is a second rank identity tensor. The definition of $X^{ss'}$ can be expressed as follows

$$X^{ss'} = h^{ss'} + h_{bs}^{ss'} + \mathbf{C}^c \cdot \mathbf{m}^{c,s} \otimes \mathbf{m}^{c,s'} \tag{10}$$

The crystallographic texture evolution calculation is given below in Eq. (11) and Eq. 12

$$\mathbf{W}^{p,c} = \sum_s \dot{\gamma}^{c,s} \mathbf{q}^{c,s} \tag{11}$$

The tensor $\mathbf{q}^{c,s}$ is the unit slip system tensor ($\mathbf{q}^{c,s} = 0.5(\mathbf{b}^{c,s} \otimes \mathbf{n}^{c,s} - \mathbf{n}^{c,s} \otimes \mathbf{b}^{c,s})$), and $\mathbf{W}^p$ is the plastic rotation rate for each crystal.

$$\mathbf{W}^c = \mathbf{W}^{app} + \boldsymbol{\Pi}^c - \mathbf{W}^{p,c} \tag{12}$$

where $\mathbf{W}^{app}$ is the macroscopically applied rotation rate and $\boldsymbol{\Pi}$ is the reorientation contribution from the anti-symmetric part of the Eshelby tensor (Lebensohn and Tomé, 1993). $\mathbf{W}^c$ is the lattice rotation rate, which is used to update the crystal orientation and texture evolution.

4.2. The twinning model

Deformation occurs in stages, starting with nucleation, then propagation, followed by thickening (Beyerlein et al., 2014; Beyerlein and Kumar, 2019). The stresses calculated within the EPSC framework are, however, grain-averaged stresses, which in standard form cannot provide the driving forces for twin nucleation or propagation. In cases where deformation twinning is profuse (e.g., >15–20% twin volume fraction) multi-scale models have been put forth, wherein separate full field calculations for intra-granular stresses were used to inform, self-consistent schemes for nucleating and growing twins (Kumar et al., 2017a; Niezgoda et al., 2014). In the material studied in this work, the total twin volume fraction is small (<5%), and we, therefore, adopt the commonly used pseudo-slip modeling approach for identifying twinning and a relatively recent method for treating lattice reorientation by twinning.

Modeling first formation of twinning within an untwinned grain by the pseudo-slip approach means that the shear provided by twinning is governed by a critical resolved shear stress and no lattice reorientation is involved. This method identifies when twinning first occurs and the predominant twin system (PTS) on which it occurs, as the twin system with the highest shear-rate among the six variants. Second, as deformation proceeds, the accumulated shear provided by the PTS may exceed a threshold value when the pseudo slip model no longer is reasonable and lattice reorientation associated with PTS activity is invoked. As is common in these models to set this threshold as 0.1, i.e., 10% accumulated shear.

Upon reaching this threshold, the parent grain is then considered *twinned* and consequently, the crystallographic re-orientation caused by the twin is modeled via the composite grain (CG) approach (Beyerlein and Tomé, 2008; Knezevic et al., 2015). In the present model, different twin variants and even twin types are allowed to form in the same grain at the same time. In the CG approach, the original grain is replaced by two separate ellipsoidal inclusions, one representing the matrix and the other the twin, and their combined volume fractions equal that of the original parent grain. The shape of these two inclusions are initially assigned to be flat ellipsoids with their short axis perpendicular to the twinning plane, to reflect the lamellar shape of newly formed twins and to change in the shape of the intervening matrix regions. The twinned inclusion adopts a mirror orientation with respect to the orientation of the parent grain that is characteristic of the type of twin. In all grains, the twinned regions are equally spaced and have equal thickness.

The volume fraction of the twin inclusion in the grain increases with twin shear activity. The shear deformation $\Delta\gamma^{tw}$ provided by twinning is localized within the twin inclusion. Because twins provide a characteristic shear S per unit volume, the increment in twin volume fraction and increment in shear are related following

$$f^s = \Delta\gamma^{tw}/S$$

where $\Delta\gamma^{tw}$ is the shear strain contributed by the twinning PTS in the grain. The characteristic shear S is 0.175 for the extension twin $\{10\bar{1}2\}\langle\bar{1}011\rangle$ and 0.218 for the contraction twin $\{11\bar{2}2\}\langle11\bar{2}3\rangle$. Modeling twin growth is taken into account by a volume fraction transfer scheme from the parent grain to the twin domain. Since the total volume fraction of the original grain does not change, as the volume fraction of the twin increases, the volume fraction of the corresponding parent grain is reduced by the same amount.

4.3. Dislocation density hardening law

For hardening on individual slip systems, a dislocation density based hardening model is employed. The basic model was first developed in Beyerlein and Tomé (2008) for HCP Zr, and over the years, this law has been successfully applied to many other metals, bearing different structures, not only HCP, but also orthorhombic, FCC, and BCC. Recently, Zecevic and Knezevic, (2015) extended the hardening model to include reversible dislocation motion and backstress evolution and this most recent model is the one adopted here. A brief review of their formulation is presented below since it introduces material parameters for each mode of slip that we will characterize for CP-Ti in this work.

In the following, α will be used to denote a family of slip systems, while $s \in \alpha$ will denote an individual slip system belonging to family α. Similarly, β denotes the twin type, and $t \in \beta$ denotes the twin system t contained in mode β.

The slip resistance, τ_c^α, which evolves with dislocation density, for any slip system $s \in \alpha$, is defined as:

$$\tau_c^\alpha = \tau_{0,f}^\alpha + \tau_{0,HP}^\alpha + \tau_{for}^\alpha \tag{13}$$

where $\tau_{0,f}^\alpha$ is the initial slip strength that does not evolve with strain. As such, this initial slip strength predominantly affects the initial flow strength. The strength $\tau_{0,f}^\alpha$ includes any effect of grain size, since in this work, samples with different average grain sizes were not considered. $\tau_{0,HP}^\alpha$ represents the barrier effect on slip imposed by the twin boundaries, and τ_{for}^α is the forest term. When twin lamellae are present in the grain, the term $\tau_{0,HP}^\alpha$ corresponds to the effect of two adjacent twin boundaries. The latter two quantities are given in turn by the following expression

$$\tau_{0,HP}^\alpha = \mu H P^{\alpha\beta} \sqrt{b^\alpha \Big/ d_{mfp}^{s,PTS}},\ s \in \alpha \text{ with a } \beta\text{-type PTS} \tag{14}$$

$$\tau_{for}^\alpha = b^\alpha \chi \mu \sqrt{\rho^s{}_{tot} + \sum_{s'} L^{ss'} \rho^{s'}{}_{tot}},\ s \in \alpha \tag{15}$$

where χ is the dislocation interaction coefficient, which usually ranges within 0.1–1.0. Here, we assign $\chi = 0.9$, and do not use it as a

fitting parameter. In the complete the formulation, $L^{ss'}$ is the latent hardening matrix. $HP^{\alpha\beta}$ is a dimensionless Hall-Petch-like coefficient that reflects the interaction between the type of slip α and type of twin boundary corresponding to the twin system(s) in the grain (Beyerlein and Tomé, 2008). It provides a hardening contribution to the macroscopic curve in the event that twins develop in the grain.

The d_{mfp} is the directional mean free path. It evolves with twin fraction to a minimum of $d_{mfp} = (d_c - d_t)/sin(\alpha)$ in the matrix or $d_{mfp} = d_t/sin(\alpha)$ in the twin, where α is the angle between the slip plane and the plane of the PTS, d_c is the center-to-center spacing between neighboring twins, d_t is the twin width, and d_g is the grain size. As in (Proust et al., 2007), we set $d_c = 0.2d_g$ for extension twins, which tend to be relative thick, and $d_c = 0.05d_g$ for contraction twinning, which tend to be comparatively finer.

In the model, two types of dislocation densities evolve with deformation: forest dislocations and reversible dislocations. For each slip system plane normal, a positive direction of slip can be assigned *a priori*, which automatically defines the negative direction. For the purposes of developing a evolution law for the reversible dislocations, each slip system s is further designated as either s^+ or s^-, corresponding respectively to slip in the positive or negative direction.

First is ρ^s_{for}, the forest dislocation density common to both the s^+ and s^- directions. Next are the $\rho^{s^+}_{rev}$ and $\rho^{s^-}_{rev}$ densities, which are the reversible dislocations associated with slip systems s^+ and s^-, respectively. They are related according to

$$\rho^s_{tot} = \rho^s_{for} + \rho^{s^-}_{rev} + \rho^{s^+}_{rev} \tag{16}$$

$$\frac{\partial \rho^s_{for}}{\partial \gamma^s} = (1-p)k_1^\alpha \sqrt{\rho^s_{tot}} - k_2^\alpha(\dot{\varepsilon}, T)\rho^s_{for},\ s \in \alpha \tag{17}$$

where k_1^α is a rate-insensitive coefficient for dislocation storage by statistical trapping of mobile dislocations and predominantly affects the initial hardening rate or stage II hardening. The parameter p is a reversibility fraction, lying between 0 and 1. It attributes the fraction of changes in the total dislocation density $(k_1^\alpha \sqrt{\rho^s_{tot}})$ to the increment in reversible dislocation density $(pk_1^\alpha \sqrt{\rho^s_{tot}})$. Here, we assign $p = 0.1$. k_2^α is a rate-sensitive coefficient for the rate of dynamic recovery and is given by

$$\frac{k_2^\alpha}{k_1^\alpha} = \frac{\chi b^\alpha}{g^\alpha}\left(1 - \frac{kT}{D^\alpha b^3} ln(\dot{\varepsilon} / \dot{\varepsilon_0})\right) \tag{18}$$

where k is Boltzmann's constant ($1.38 \times 10^{-29}\ MPa\, m^3/K$), D^α is a drag stress, and g^α is the effective activation enthalpy. The pre-factor $\dot{\varepsilon_0}$ has units of strain rate and is related to the frequency of thermal fluctuations, which is a fraction of the Debye frequency. As in prior works on polycrystalline metals, it is taken to be $10^7/s$. The dynamic recovery process is often associated with dislocation processes, such as cross slip and climb, which enable closely spaced dislocations to migrate short distances and annihilate. It tends to affect the transition from stage II to stage III hardening.

The reversible dislocation density populations evolve with a particular direction of shearing. Specifically when the direction of shearing is positive, $d\gamma^{s^+} > 0$, then

$$\frac{\partial \rho^{s^+}_{rev}}{\partial \gamma^{s+}} = pk_1^\alpha \sqrt{\rho^s_{tot}} - k_2^\alpha(\dot{\varepsilon}, T)\rho^{s^+}_{rev} \tag{19}$$

$$\frac{\partial \rho^{s^-}_{rev}}{\partial \gamma^{s+}} = -k_1^\alpha \sqrt{\rho^s_{tot}} \left(\frac{\rho^{s^-}_{rev}}{\rho^{s^-}_0}\right)^m \tag{20}$$

where m is the parameter controlling the rate of dislocation recombination, and set as $m = 0.6$. The ρ^s_0 is the total density that was present when the shear is reversed on the s^{th} slip system. When the direction of shearing is negative, i.e., $d\gamma^{s^-} > 0$, the increment in $\rho^{s^-}_{rev}$ is analogous to Eq. (19), while the increment in ρ^{s^+} is equal to that of Eq. (20).

Finally, the evolution in the slip resistance τ^s_c with strain described above in Eq. (13) is related to instantaneous hardening coefficients $h^{ss\prime}$ used in Eq. (6) via

$$h^{ss'} = \partial \tau^s_c / \partial \gamma^{s'} \tag{21}$$

The evolution of the backstress on a slip system is done via instantaneous hardening coefficients defined as:

$$h^{ss'}_{bs} = \partial \tau^{bs}_s / \partial \gamma^{s'} \tag{22}$$

4.4. Backstress evolution law

Here we adapt the slip-level backstress evolution law introduced in (Zecevic and Knezevic, 2015) for an FCC aluminum alloy to HCP CP-Ti. The law presumes that backstresses develop as dislocations accumulate with strain. Backstresses are directional and depend on the sense of shear responsible for storing or releasing dislocations in the crystal. Dislocations gliding in one direction can generate backstresses that resist slip in the same sense of direction but aid slip in the opposite sense. A positive backstress on slip system s acts against it and a negative backstress on s acts in favor of it.

The backstress model is briefly reviewed here for the purposes of introducing the associated parameters and readers interested in more detail can refer to (Zecevic and Knezevic, 2015). When slip is activated on the s^+ system, i.e., $d\gamma^{s^+} > 0$, then the backstress $\tau_{bs}^{s^+}$ evolves according to:

$$\tau_{bs}^{s+} = \tau_{bs}^{sat}(1 - exp(-\nu\gamma^{s+})) \tag{23}$$

The strain γ^{s+} also generates a negative backstess $\tau_{bs}^{s^-}$ on the slip system s^-.

$$\tau_{bs}^{s^-} = -A\tau_{bs}^{s^+} \tag{24}$$

The value of A is an asymmetry parameter and ν controls the rate at which the backstress reaches the saturation value τ_{bs}^{sat}. When $A = 1$, then backstresses caused by $d\gamma^{s+} > 0$ generate an equal but negative backstress on s^-. If the stress available to re-emit or re-mobilize piled up dislocations is larger than that which resists them, then A will be larger than unity but is generally of order $10^0 - 10^1$.

In reversal, the slip system s^- becomes active, $d\gamma^{s^-} > 0$, and the backstress $\tau_{bs}^{s^+}$ decays from the value $\tau_{bs0}^{s^+}$ accumulated at the point of reversal. Physically, this reduction is interpreted as dislocations once piled up are now reemitted or remobilized in reverse. The empirical function governing this decay is given by:

$$\tau_{bs}^{s^+} = -A\tau_{bs}^{s^-} \tag{25}$$

and

$$\tau_{bs}^{s^-} = -(A+1)\tau_{bs0}^{s^+} exp(-\frac{\gamma^{s^-}}{\gamma_b}) + \tau_{bs0}^{s^+} \tag{26}$$

where the rate of decay is governed by γ_b. The parameters A, ν, and γ_b are related to dislocation accumulation and the stress fields produced by clusters of them. As such, we assume they depend on the type of dislocation, and hence differ among slip modes but are the same for individual systems belonging to the same mode.

4.5. Resistance to twin propagation

The model assumes a twin resistance to twin propagation calculated in the model as a critical value of the shear stress resolved in the twin direction and twin plane. This critical threshold for twin system t in twin mode β consists of the sum of two different terms:

$$\tau_c^t = \tau_0^\beta + \tau_{slip}^\beta \quad t \in \beta \tag{27}$$

In Eq. (27), and the following equation, β represents the twin mode. The first term τ_0^β is the propagation resistance without interactions with other dislocations and the resistive effects of grain or twin boundaries. The twin variants that lie in the grain as reoriented lamellae are referred to as predominant twin systems (PTSs).

The second term in Eq. (27) represents the contribution to hardening for all twin systems due to interactions with slip dislocations. It can increase proportionally with the dislocation population according to

$$\tau_{slip}^\beta = \mu \sum_\alpha C^{\alpha\beta} b^\beta b^\alpha \rho^\alpha \tag{28}$$

where μ, b^β, and $C^{\alpha\beta}$ are the elastic shear modulus on the system, the magnitude of the Burgers vector for the twinning dislocation, and the twin-slip interaction matrix (Knezevic et al., 2013; Beyerlein and Tomé, 2008; Yoo and Loh, 1970). Slip dislocations can either promote or hinder twin propagation. Positive values of $C^{\alpha\beta}$ indicate when the accumulation of slip dislocation retards and eventually surpasses twin growth, and negative when slip dislocations aid twin dislocation generation.

4.6. The detwinning model

In the event that the deformation in the grain is reversed, detwinning of the PTS could occur. The detwinning model monitors the possible activation of the PTS inside the twin inclusion (i.e., twinned region), as well as the other twin variants that are not yet represented as reoriented twin inclusions. If another variant other than the PTS is activated, then a secondary twin is created inside the twin inclusion. The detwinning process initiates when the PTS becomes activated inside the twin inclusion. The volume occupied by the PTS is then transferred from the original twin to the matrix. This process is permitted to continue until the entire twin volume has been transferred back to the parent grain, at which point the grain is twin-free and the twin inclusion removed. To prevent the other twin variants inside the twinned region from being activated once the detwinning process has started, their twin resistance is assigned an exceptionally high value (Knezevic et al., 2013a). Last, we mention that the initial detwinning resistance, τ_{prop}^β, is made equal to the τ_0^β in twinning process. The contribution of the surrounding dislocations on evolution of the detwinning resistance follows the same law as for twinning. The final expression for the detwinning resistance is

$$\tau_c^{\beta} = \tau_{prop}^{\beta} + \mu \sum_{\alpha} C^{\alpha\beta} b^{\beta} b^{\alpha} \rho_{for}^{\alpha} \tag{29}$$

4.7. Model set up for load reversals

The polycrystal is represented by a set of grains that have an ellipsoidal shape with crystal orientation and volume fraction. The slip systems and twinning families made available in the simulation are listed in Table 1. These five slip and twinning families have been reported in experimental studies of CP-Ti (Won et al., 2015, 2017; Hosford, 1993; Warwick et al., 2012; Chichili et al., 1998). They have also been used as input into prior simulation studies on CP-Ti, such as in CPFE (Hama et al., 2016), and VPSC (Wronski et al., 2018) and proven capable of modeling the main deformation characteristics in monotonic deformation (Wu et al., 2008; Wronski et al., 2018). The initial dislocation density are set to $5.55 \times 10^{10}/m^2$. The latent hardening matrix $L^{ss'}$ components in Eq. (15) are 0.5 for interactions between dissimilar slip modes and 1.0 for interactions between slip systems belonging to the same slip mode. The strain rates are set to be the same as the experiment ($6.67 \times {}^{-4}s^{-1}$). The single-crystal elastic constants used for α-Ti were: $C_{11} = 162.4$ GPa, $C_{12} = 92$ GPa, $C_{13} = 69$ GPa, $C_{33} = 180.7$ GPa, and $C_{44} = 46.7$ GPa (Simmons and Wang, 1971).

The initial texture measured experimentally in Fig. 4 was used to build the initial texture to be used in all simulations. Fig. 1 shows the pole figures of the model initial texture, which agrees with the measurement, particularly in the main texture components.

Load reversal tension-compression and compression-tension tests were simulated by imposing strain increments along RD or TD, while enforcing zero average stress in the ND and the other lateral sample direction. Using an average stress of 9 MPa in the ND as in the experiment instead of zero MPa had negligible effect on the results. In simulation, the dislocation density and grain shape and texture were continuously updated.

To characterize the material parameters associated with the hardening law for slip and the model for twinning and detwinning, we compared the simulated forward-reverse stress-strain responses with the experimental responses associated with the 5% cyclic strain tests in the RD and TD directions. The parameter sets for the slip and twin hardening parameters are given in Tables 2 and 3, respectively. Requiring that a single set of parameters in the model can reproduce the stress-strain responses in all load reversal tests highly constrains the range of parameters that can be used and, therefore, is a strong indication that these parameter sets are reliable. As validation, the same material parameters were then used to predict the 2%, and 10%-strain load-reversal tests. Finally, the model is used to calculate the deformation textures, twin volume fraction evolution, and underlying contributions of each slip and twinning mode with strain in all available 2%, 5% and 10% load reversal strain tests.

5. Results

5.1. Stress-strain response

The model is first used to understand the slip, twinning, and slip-twin interactions that underlie the measured cyclic loading responses. Fig. 2 and 3 compares the calculated curves with the measured ones for all the 5% forward-reverse loading tests. As shown, the model replicates well the forward and reload deformation responses, including the lower yield stress on reverse straining than in pre-straining and hardening rate.

A few aspects of the deformation response are worth noting. The material exhibits a small amount of tension-compression asymmetry in yield and strain hardening. In the RD, for instance, the yield stress and flow stress at 5% in monotonic compression are 202 MPa and 406.5 MPa, whereas they are 198 MPa and 422.3 MPa in monotonic tension. The response also exhibits a Bauschinger effect, wherein the yield stress in the tension reload is 161 MPa, compared to the 202 MPa in the compression pre-straining step. The responses are generally higher in the TD-load tests compared to the RD-load tests. For instance, after 5% compression loading in the TD, the yield and flow stress are 221 MPa and 429 MPa. Notably, these features are also represented in the calculated stress-strain responses.

5.2. Slip model strengths and dislocation density rate parameters

The material parameter set associated with these calculations can provide some insight into individual slip strengths and their tendencies for strain hardening. Tables 2 and 3 present the material parameters corresponding to the rate laws for dislocation density evolution and twinning, and kinematic hardening. Although they were able to simultaneously match all load-reload tests in Fig. 2 well,

Table 1
Slip and twinning modes used in this work for CP-Ti

Mode	Symbol	Crystallography	No. of systems	b(Å)
Prismatic$\langle a \rangle$	$\alpha = 1$	$\{10\bar{1}0\}\langle\bar{1}2\bar{1}0\rangle$	3	2.95
Basal$\langle a \rangle$	$\alpha = 2$	$\{0001\}\langle11\bar{2}0\rangle$	3	2.95
Pyramidal$\langle a + c \rangle$	$\alpha = 3$	$\{10\bar{1}1\}\langle\bar{1}\bar{1}23\rangle$	12	5.54
Extension Twinning	$\beta = 1$	$\{10\bar{1}2\}\langle\bar{1}011\rangle$	6	0.3017
Contraction Twinning	$\beta = 1$	$\{11\bar{2}2\}\langle11\bar{2}3\rangle$	6	0.2725

Table 2
Hardening parameters for CP-Ti

	Prismatic($\alpha=1$)	Basal($\alpha=2$)	Pyramidal($\alpha=3$)
$\tau_0^\alpha[MPa]$	69	128	180
$k_1^\alpha[m^{-1}]$	1.02×10^8	1.07×10^8	0.95×10^8
g^α	0.01	0.015	0.09
$D^\alpha[MPa]$	500	800	800
$HP^{\beta=1}$	0.1	0.1	0.1

	$\tau_0^\beta[MPa]$	$C^{1\beta}$	$C^{2\beta}$	$C^{3\beta}$
Extension Twin ($\beta=1$)	230	20000	8600	11200
Contraction Twin ($\beta=2$)	260	8200	8200	8000

Table 3
Kinematic hardening parameters for CP-Ti

	$\tau_{bs}^{sat}[MPa]$	ν	γ_b	A
Prismatic($\alpha=1$)	11	40	0.001	1
Basal($\alpha=2$)	15	60	0.006	1
Pyramidal($\alpha=3$)	15	50	0.09	5

it is recognized that they may not be unique. For this reason, we compare these parameters with similar material parameters reported in the literature as well as perform validation calculations.

The initial slip resistance τ_0, given in Table 2, governs the initial yield stress and is a common parameter in most hardening models. In the present case, prismatic $\langle a\rangle$ slip has the lowest initial slip resistance, basal $\langle a\rangle$ slip has the next higher one, and pyramidal $\langle c+a\rangle$ slip the highest. The values are in good agreement with CRSS measurements made by in-situ high energy X-ray diffraction microscopy (HEDM) experiment, which reported 96 ± 18 MPa for prismatic $\langle a\rangle$ slip and 127 ± 33 MPa for basal $\langle a\rangle$ slip (Wang et al., 2017). Also, in agreement, pyramidal $\langle c+a\rangle$ slip was reported to have the highest CRSS; however, it was indirectly assessed to be larger than 240 MPa, which is larger than that found here. The ranking of these modes is also consistent with slip strengths from many other studies, which involved experimental data and modeling approaches different from ours (see recent review in Britton et al., 2015) as well as those from recent modeling work on CP-Ti by Wronski et al. (2018), which used the same dislocation density based law as we use here, but within the visco-plastic self-consistent (VPSC) model and for modeling monotonic stress-strain response data. Also we note that among the three slip modes, the prismatic slip mode has the lowest trapping coefficient, drag stress, and activation enthalpy for dislocation processes aiding dynamic recovery. It would be expected that prismatic slip would continue to dominate plasticity in CP-Ti.

Table 3 reports the material parameters associated with the resistance to twin expansion (as opposed to nucleation). The resulting values for τ_0 for twinning suggest that both contraction and extension twinning are more difficult to propagate compared to slip, with contraction twinning being the slightly harder one of the two modes. The relative ease of $\{10\bar{1}2\}$ extension twinning compared to $\{10\bar{1}\bar{1}\}$ contraction twinning is consistent with experimental assessments by Tirry et al. (2012). We also observe from Table 3 that the interaction matrix $C^{\alpha\beta}$ components are relatively large, indicating a strong repulsive interaction between these two twin types and all types of dislocations.

For validation, the model is applied to additional load reversal tests involving either lower (2%) strains or higher (10%) strains (Hama et al., 2015), without further adjustments to the parameters in Tables 2 and 3 The comparison between the simulated and measured responses given in Fig. 2 show that the model achieves reasonable agreement.

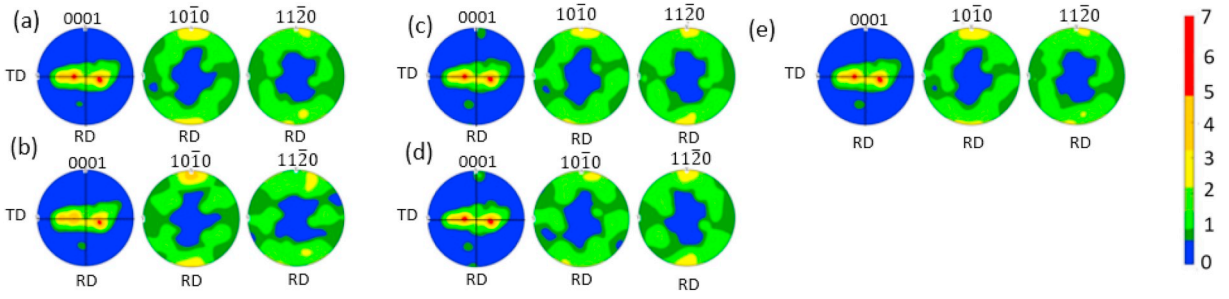

Fig. 5. Calculated textures presented as {0001} pole figures for the (a) initial texture and (b–e) deformed RD samples: (b) texture at 0.1 strain during the tension in TC loading (c) texture at −0.1 strain during compression in CT loading, (d) and (e) textures at −0.05 and 0 strain, respectively during reverse loading in CT loading.

6. Deformation mechanisms

Another important output of the modeling effort is the active slip and twin modes underlying each cyclic test and their individual contributions to the overall polycrystalline deformation. Experimental assessment of which slip and twinning systems are active during deformation can be challenging. Common approaches involving metallography are post-mortem methods and they indicate the types of dislocations that are stored (Kumar et al., 2017b; Lentz et al., 2014; Han et al., 2012; Zheng et al., 2014). In-situ approaches utilizing diffraction involve a model to de-convolute or decouple the relative amounts contributed by the active slip and twinning systems (Zhang et al., 2019; Risse et al., 2017; Lentz et al., 2015). In this section, we make use of the model to provide some insight into the strain evolution of slip activity and twin volume fraction during these load reversal tests.

6.1. Slip activity

The calculated strain evolution of the relative slip activities (RA^{α}) of basal slip, prismatic slip, and pyramidal $\langle c+a\rangle$ slip for the bulk polycrystal during the 5% strain cycle are presented in Fig. 6. Relative slip activity is defined as:

$$RA^{\alpha} = \frac{\sum_{n} W_n \sum_{s} d\gamma^{s}_{\alpha,n}}{\sum_{n} W_n \sum_{\alpha}\sum_{s} d\gamma^{s}_{\alpha,n}} \tag{30}$$

where W_n is weight percentage of grain n and the calculation for slip activity spans all grains n in the polycrystal. Further, the sum $\sum_s$ is taken over all slip systems belonging to the α family and the sum $\sum_\alpha$ corresponds to the strain contributed by all modes of slip and twinning in a grain n. The slip activity plots begin where plasticity initiates in a given strain path. Between strain paths when the material is first reloaded, we note a short transient period, wherein in slip activity rapidly changes due to a combination of backstresses evolution, evolution of the elastic contribution, and initial easy glide on the easiest slip system, prismatic slip.

From the results in Fig. 6, we first notice that in RD and TD deformation, whether initially in compression or tension, that prismatic slip is the most active throughout deformation. Secondly, although prismatic slip is the dominant mechanism, the other two slip modes contribute, albeit in varying amounts. The initial texture is not uniformly random, yet it is not exceptionally strong. The basal poles of the grains are distributed within a range of 60° about the normal direction in the TD direction. It can, therefore, be anticipated that under an in-plane uniaxial stress state, many grains would be suitably oriented for both $\langle a\rangle$ slip and $\langle c+a\rangle$ slip. Thirdly, there is little tension-compression asymmetry in slip activity, provided that the loading direction is preserved. Fig. 6 shows that in either RD or TD loading, the relative activities of the three slip modes in tension and compression are the same. Last, the results indicate that slip activity during deformation is unaffected by pre-straining. Whether the load is directed in the RD or TD, the slip activity in the compression reload after tension pre-strain is similar to the slip activity in compression without the pre-straining.

Compared to the sense of loading or the order of the cyclic loading (CT vs. TC), the loading direction, whether in RD or TD, has the greatest effect on the type and amounts of slip activated. This particular plastic anisotropy is to be expected due to the fact that the material, as mentioned, not only has a preferred initial texture but it also does not exhibit symmetry in the plane of the sheet (e.g., it is not axisymmetric about the ND). Loading along the RD direction has more grains more suitably oriented for pyramidal $\langle c+a\rangle$ slip than basal $\langle a\rangle$ slip compared to loading along the TD, which activates more basal $\langle a\rangle$ slip than pyramidal $\langle c+a\rangle$ slip.

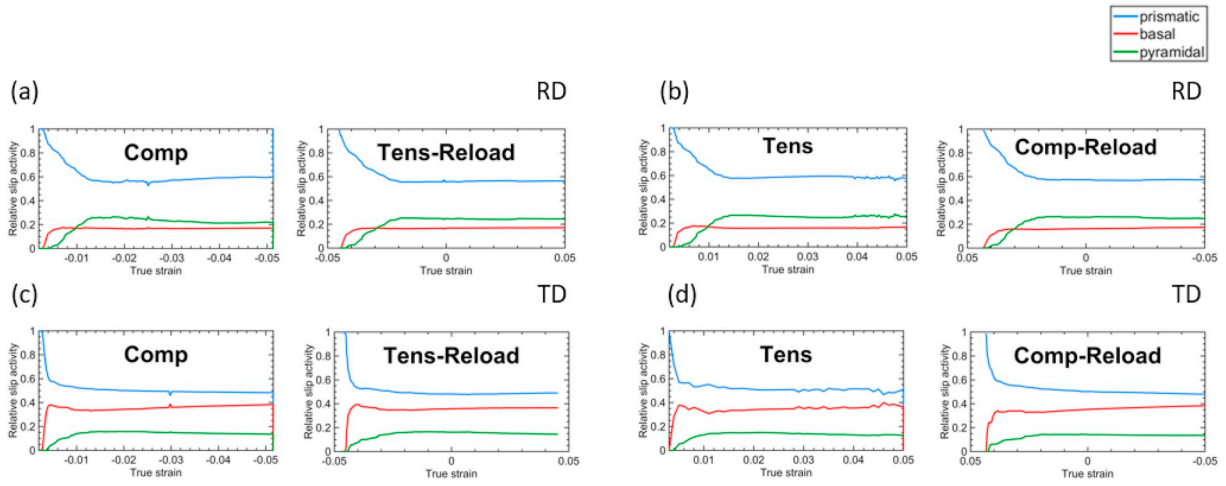

Fig. 6. Calculated slip activities during 5% cyclic loading: (a)RD-CT; (b)RD-TC; (c)TD-CT; (d)TD-TC.

6.2. Deformation twinning in RD loading

Deformation twinning, unlike slip, is a unidirectional deformation mechanism, and compared to slip, can be much more sensitive to crystallographic orientation and sense of loading (whether in compression or tension). Fig. 7(a and b) examines the strain evolution of the bulk polycrystal twin volume fraction calculated by the model during the 5% strain cyclic tests in the RD direction. The first test analyzed of our results applies compression in the RD and reloads in tension in the RD, and the second one examined takes the opposite path, with tension applied in the RD followed by compression in the RD. Initially, the c-axes of most grains in the sample are closely aligned along the ND, so compression in RD favors TTWing, whereas tension in RD favors CTWing. These two tests, therefore, enable study of the effects of the reloading path on either TTWing or CTWing generated in the preloading step.

We first consider the RD-CT cyclic test, RD compression followed by a tension reload. From the model calculations, in RD compression, TTWing is activated and increases to 3.5% twin volume fraction for the entire polycrystal by 5% compression strain. Upon unloading and reloading in tension, detwinning of the TTWs occurs. After 5% tension reloading, the TTW volume fraction is still 2.5%. No new TTWs occur in tension reloading, so the 2.5% TTW fraction at the end of the test are retained from pre-straining. In agreement, Hama et al. (2015) and Ma et al. (2019) reported $\{10\bar{1}2\}$ twinning during RD compression and $\{10\bar{1}2\}$ detwinning in the tension reload following compression. During this test, CTW also occurs but in relatively small amounts. CTWing is activated while unloading and reloading, reaching a total of 0.5% twin volume fraction after 5% tension reloading.

The model calculations for the RD-TC load reversal test, RD tension followed by a compression reload, find that twinning is not prevalent. At the end of 5% RD tension step, the calculated CTW volume fraction is 0.6% (Fig. 7). Upon unloading and reloading in RD compression, the CTW volume fraction decreases. CTW-detwinning is slow and incomplete, leaving some CTWs at the end of the test. After 10% RD tension, the calculated CTW volume fraction is higher at 1.5% (see Fig. 8(c)). TTWing did not occur in either RD tension pre-loading or RD compression reloading. In agreement, corresponding experiments (Hama et al., 2015; Ma et al., 2019) also reported that $\{10\bar{1}2\}$ twinning was more active during RD compression than during RD tension.

6.3. Comparison with texture in RD loading

Fig. 4 presents the texture measurements reported previously in Hama et al. (2015), wherein they used only $\langle 0001\rangle$ and $\langle 10\bar{1}0\rangle$ pole figures. The texture in Fig. 4(b) for RD tension after 10% strain presents little change in the basal pole figure from the initial texture. The prismatic poles have aligned along the RD, the tensile loading direction. This evolution would be expected of slip dominated deformation. Consistent with this assessment, the model predictions for this case indicate that monotonic RD tension is accommodated predominantly by prismatic slip and little CTWing (1.5% twin volume fraction, see Fig. 7). The calculated texture for this case agrees with the experimental measurement (see Fig. 5).

Texture measurements were also made in RD-compression testing. The measured textures in Fig. 4(d) after 5% compression straining and in Fig. 4(c) after 10% present evidence some TTWing. The basal pole figure displays a weak basal pole texture component aligned with the RD that is not found in the initial texture. This change is a common signature of TTWing, which can reorient the basal pole 85–86° toward the loading axis. The fact that it is weak is consistent with the prediction that the TTW volume fraction after 5% is 3.5% and after 10% is 4.1%. The measured texture in Fig. 4(e) at zero net strain, achieved during the tension reload step, shows that this "twinning signature" has disappeared, implying detwinning. In agreement the calculated texture in Fig. 5 also predicts disappearance of this component. Further, for this same zero net strain the calculated TTW volume fraction has reduced to 3% as a result of

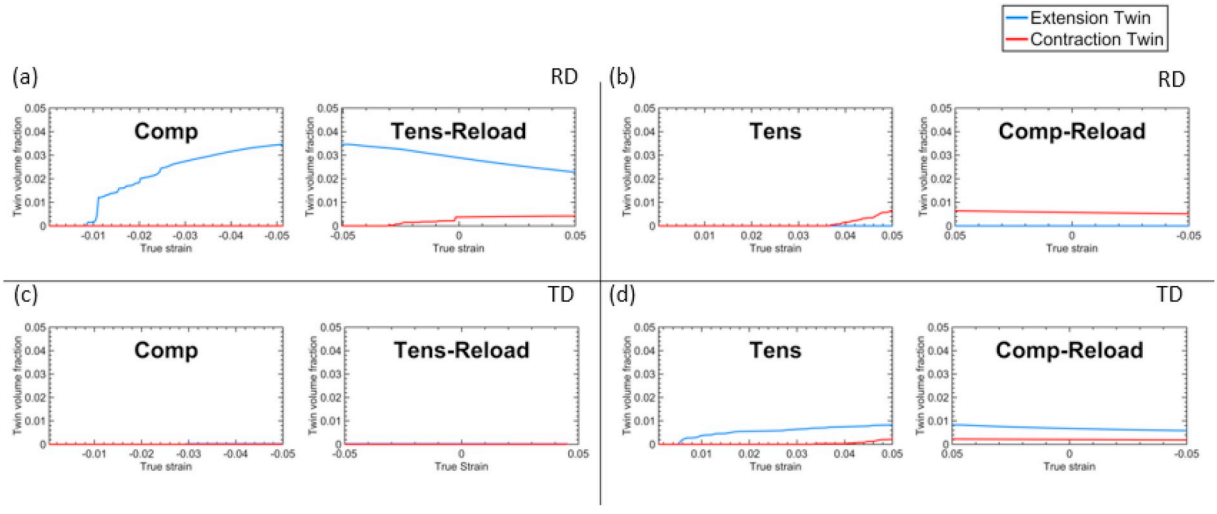

Fig. 7. Calculated twin volume fraction evolution during 5% cyclic loading in (a–b) RD and (c–d) TD directions: (a)RD-CT; (b)RD-TC; (c)TD-CT; (d) TD-TC.

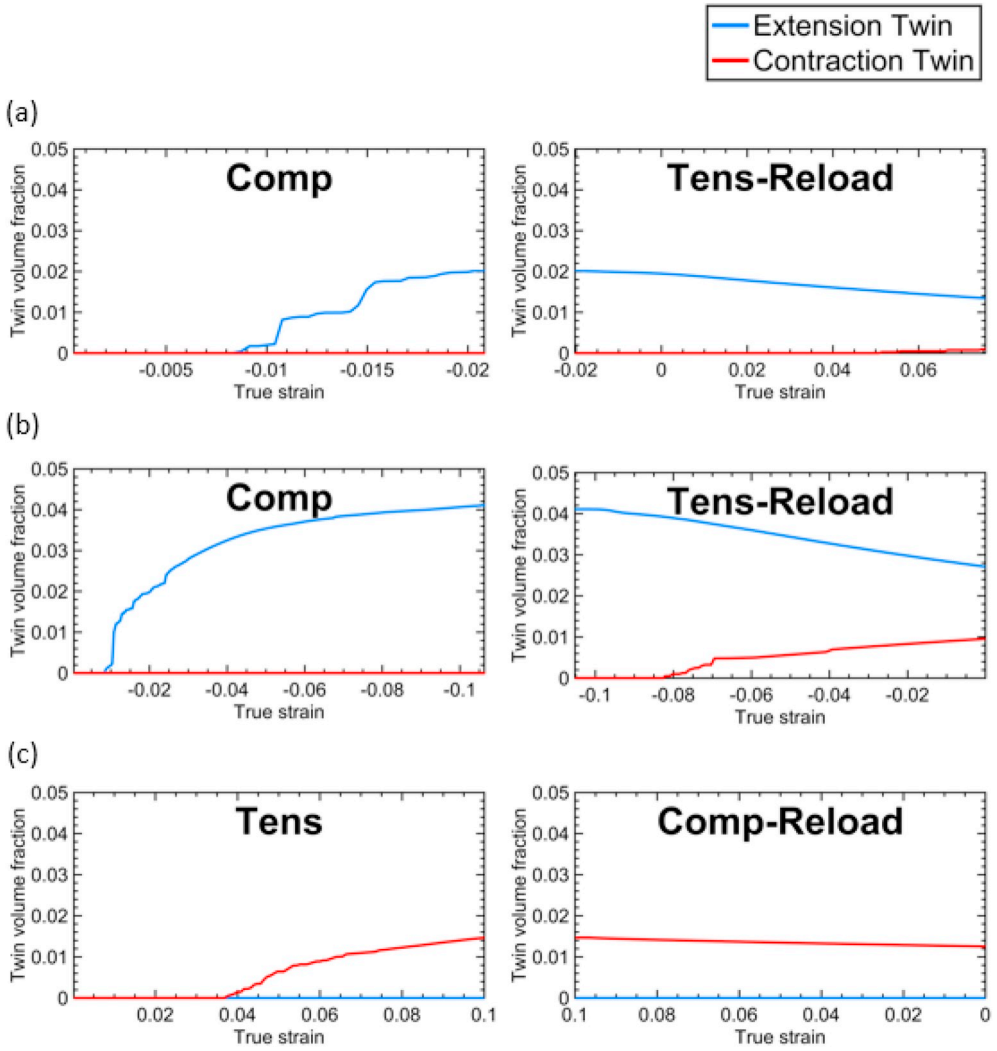

Fig. 8. Calculated twin volume fraction evolution during cyclic loading:(a)2% RD-CT, (b)10% RD-CT and (c)10% RD-TC.

detwinning.

6.4. Deformation twinning in TD loading

Fig. 7(c and d) shows the strain evolution of extension and compression twin volume fraction in the two cyclic tests applied along the TD direction of the sheet. Unlike in RD loading, in TD loading, deformation twinning is negligible, highlighting the strong anisotropy caused by the initial texture. In TD-CT loading, twinning is not activated, and in TD-TC loading, small amounts of extension twins (<1% volume fraction) are produced during the forward tension path. After 0.04% strain, contraction twinning initiates and grows to negligible amounts (<< 1% volume fraction). During the compression reload, these twins are largely preserved, with no further propagation and negligible occurrences of detwinning. To conclude, in TD, deformation is largely slip dominated, indicating that any hysteresis seen in the cyclic stress-strain response is due to the development of backstresses. This finding is in good agreement with the conclusion in Hama et al. (2015) and Ma et al. (2019) that the activity of twinning is much smaller in TD than in RD (2015).

7. Discussion

7.1. Effect of backstress development

To analyze backstress development, the backstress of each slip system in each grain during deformation is calculated. Fig. 9 presents the backstress (type III stress) averaged over the entire polycrystal. While backstresses may develop in all slip systems, only the top two slip systems generating the most backstress in each test are shown. Overall, their value is small relative to the flow stress,

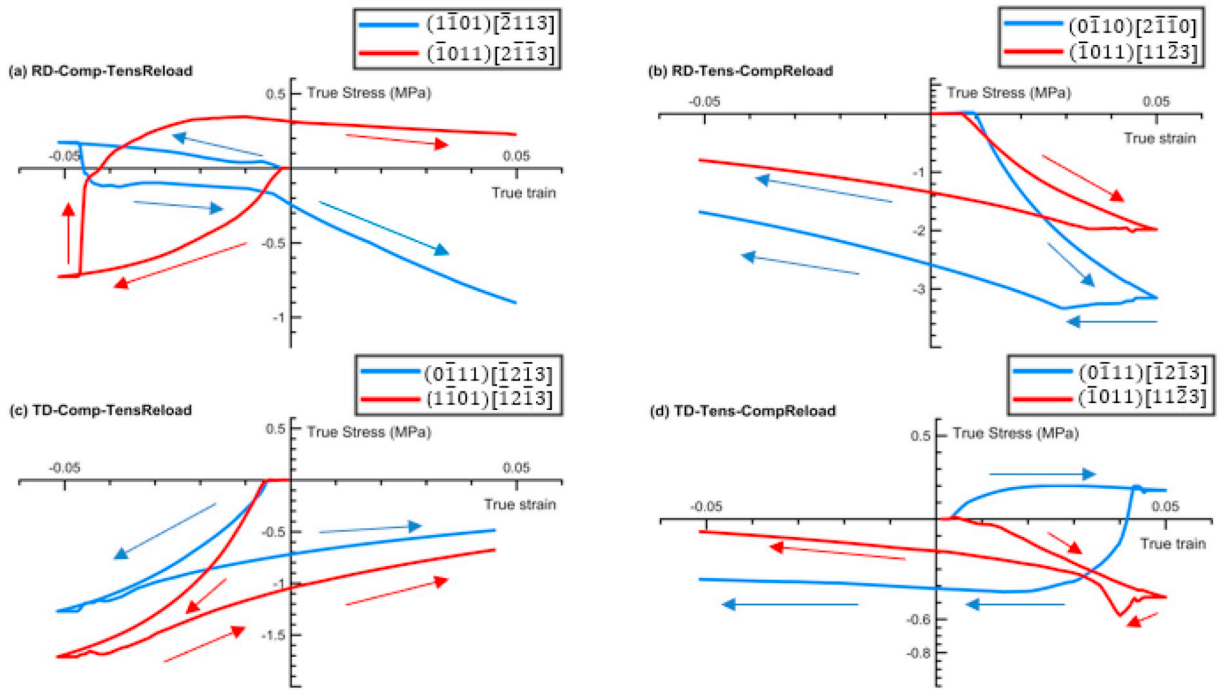

Fig. 9. Calculated backstress evolution in the two slip systems developing the highest backstress values in each cyclic test.

which is expected for intra-granular stresses (type III stress). In Fig. 9, we observe that the backstress evolves abruptly with small changes in strain. Its value increases with strain, remains constant with unloading, and drops in reloading. The model indicates that in the four tests studied here, the backstress develops predominantly on a few pyramidal slip systems, experiencing the largest slip activity. For instance, in the CT test in the RD direction, the top two systems are the (1$\bar{1}$01)[$\bar{2}$113] and ($\bar{1}$011)[2$\bar{1}\bar{1}$3] pyramidal slip systems, while for the TD-TC test they are (0$\bar{1}$11)[$\bar{1}$2$\bar{1}$3] and ($\bar{1}$011)[11$\bar{2}$3] pyramidal slip systems. The amount of backstress on these systems loosely correlates with the amount of pyramidal slip activity in the test. The RD-TC test generates the most backstress among the four tests, wherein pyramidal slip was the second most active slip system, compared to prismatic slip, and among the four tests, pyramidal slip was the most active.

The active slip and twinning systems in each grain are determined by a combination of the backstress and local stress resulting from the applied strain. Further, we note that the backstresses are relatively small (<4 MPa) compared to the macroscopic stress. In an attempt to elucidate the individual role played by the backstress, we repeat the calculations without the backstress model and study the resulting slip and twinning activity. We first re-characterize a few material parameters in the dislocation density law to ensure that the

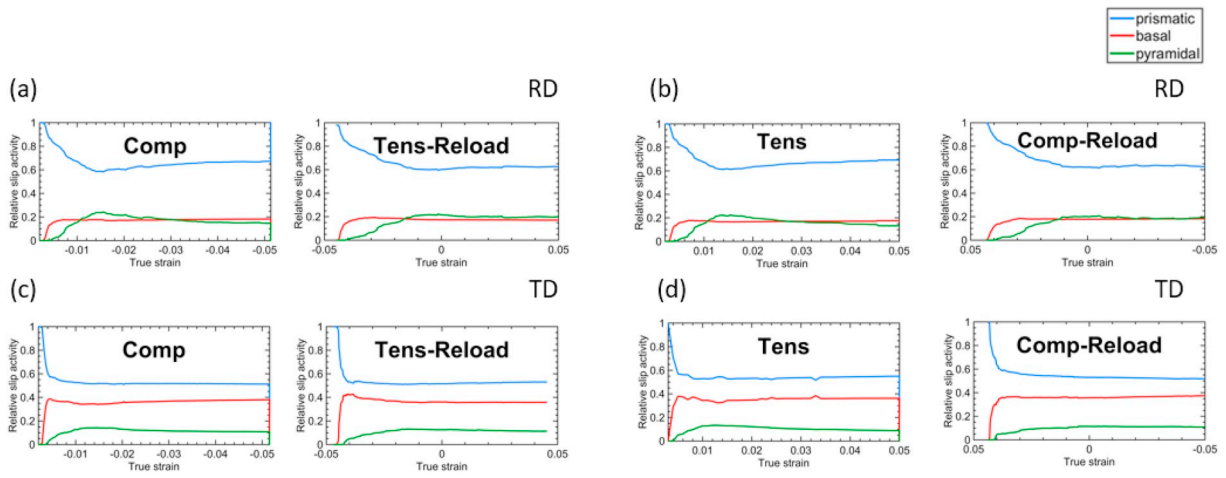

Fig. 10. Calculated slip activities of the mode without taking into account backstress development during 5% cyclic loading in RD and TD directions: (a)RD-CT; (b)RD-TC; (c)TD-CT; (d)TD-TC.

model without backstress develop can still replicate the forward stress-strain response. Toward this end, only k_1^α and g^α for the prismatic slip mode needed to be changed to 1.22×10^8 and 0.025, respectively. Fig. 10 and Fig. 11 show the slip activity and twin volume fraction evolution in the load reversal test without backstress development included. Compared to the case without backstress, we find that TTW development has reduced during the initial compression deformation and CTW has been suppressed entirely. Pyramidal slip, TTW and CTW are all modes that accommodate $\langle c \rangle$ axis deformation in the grains. This analysis indicates that backstress, which develops preferentially on the pyramidal slip systems, hinders pyramidal slip, thereby encouraging the formation of twins.

7.2. Effect of preloading

The model analysis indicates that, at the polycrystal scale, the amounts of each slip mode that contribute to the deformation are not significantly affected by the sense of direction—tension or compression—or by the 5% pre-straining. Comparatively, however, the strain path change is seen to noticeably affect deformation twinning. In the 5% deformation cycle, TTWing was activated in RD compression at 5% deformation with no prestraining but it was not activated during RD compression after 5% deformation following RD-tension prestraining step to 5% deformation. Similarly, CTWing was activated in RD tension after 5% straining with no pre-straining step but not when RD tension was applied after a RD compression pre-straining step. This suggests that marked differences in twinning activity between monotonic loading and cyclic loading can be expected even in HCP materials that twin easily.

Much of the analysis, thus far, has focused on load reversal tests to 2% and 5%. We next apply the model to predict the effect of the pre-straining primary path on the reversal compression or tension response in the RD direction, by comparing the response up to 10% strain without and with 5% prestraining and analyzing the changes in slip and twinning activity. In Fig. 12(a) we compare the RD tensile response starting from the initial texture and twin-free microstructure with the RD tensile response after 5% compression pre-straining. The results show that the tensile response has been altered by the pre-straining. Compared to the response without the compression preload, the yield stress has been reduced and the work-hardening rate increased. The model indicates that this change is not a result of a change in slip activity. As shown in Fig. 6 the slip activity in the compression reload deformation is predominated by prismatic slip and accompanied by a lower, although a substantial, contribution of pyramidal slip and basal slip. At the polycrystal level, the amounts of strain contributed by these three slip modes is similar in RD tension without and with the pre-straining (see Fig. 13). However, the twinning activity has changed. In the cyclic test case, the compression pre-strain introduces TTWs, calculated to be 3.5% volume fraction (see Fig. 7(a)). When tension is subsequently applied, the material already contains TTWs, which proceed to detwin during the course of tensile loading, and forms CTWs, which achieve about 1% CTW volume fraction after 10% tensile strain. In comparison, tensile loading from a twin-free structure develops 1.6% volume fraction after 10% tensile strain (see Fig. 14). Thus, the effect of pre-straining is to reduce the amount of twinning. Pre-straining creates a backstress on pyramidal slip, which can favor its activation when the strain is subsequently reversed.

Likewise, the effect of twin-slip interactions can be assessed when comparing the RD compression responses. In the RD direction, Fig. 12(b) compares the compression "monotonic" response, initially with a twin-free microstructure, and the compression reload response after 5% tension pre-straining. As in the other test, the compression response has been altered by the pre-straining, with a lower yield stress and higher work-hardening rate, than the compression response without the prestraining. Similarly, the change cannot be attributed to profound changes in slip activity. Both RD compression responses are accommodated by prismatic slip and secondly pyramidal and basal slip (see Fig. 6). The twinning behavior, however, has experienced a noticeable change, as shown by comparing Figs. 7 and 14. After the tensile 5% pre-strain, the material develops 0.6% volume fraction of CTWs. During the subsequent compression reload path, the CTWs do not detwin but are maintained and more significantly, no TTWing occurs. This response is in stark contrast, during the compression response without pre-straining, which develops 4.4% volume fraction of TTW after 10% straining. Again, the pyramidal slip backstress that develops in pre-straining favors pyramidal slip in the following reverse straining, making TTW less competitive.

In Fig. 13, the dislocation activities and twin volume fraction for monotonic loading are plotted. We can observe that the dislocation activity for prismatic and basal are very similar in different loading path. But during monotonic loading, pyramidal slip is activated. During CT loading process, detwinning are activated. We speculate the twinning and detwinning mechanism may compete with the pyramidal slip. The pyramidal slip has a much higher critical shear stress than basal slip and prismatic slip. Thus, it is reasonable to think the activation of pyramidal will not the major factor of lower macroscopic stress in monotonic loading simulation. Then we infer the high twin volume fraction is an explanation of the difference between MT loading and CT loading. This adhere to our former conjecture that the formation of twin result in an increase in macroscopic stress.

8. Conclusions

In the present study, we use an elasto-plastic self-consistent (EPSC) polycrystal plasticity model to study the deformation behavior in commercially pure titanium under load reversals. The model takes into account several subgrain mechanisms, anisotropic elasticity, crystal plasticity by $\{10\bar{1}0\}$ prismatic slip, $\{0001\}$ basal slip and $\{10\bar{1}1\}$ pyramidal slip, dislocation density based hardening of slip strengths, deformation twinning by both contraction and extension twinning, reorientation by twinning and detwinning, and slip-system-level backstress development. With a single set of material parameters, the model achieves good agreement with a broad range of tests: true stress-strain responses in both compression-tension and tension-compression type cycles, to different strain levels, 2%, 5%, and 10%, and repeated in two different directions, the rolling and transverse directions. The texture evolution predicted by the model agrees well with available measurements. With the model, we further investigate the slip activities, twin activities and

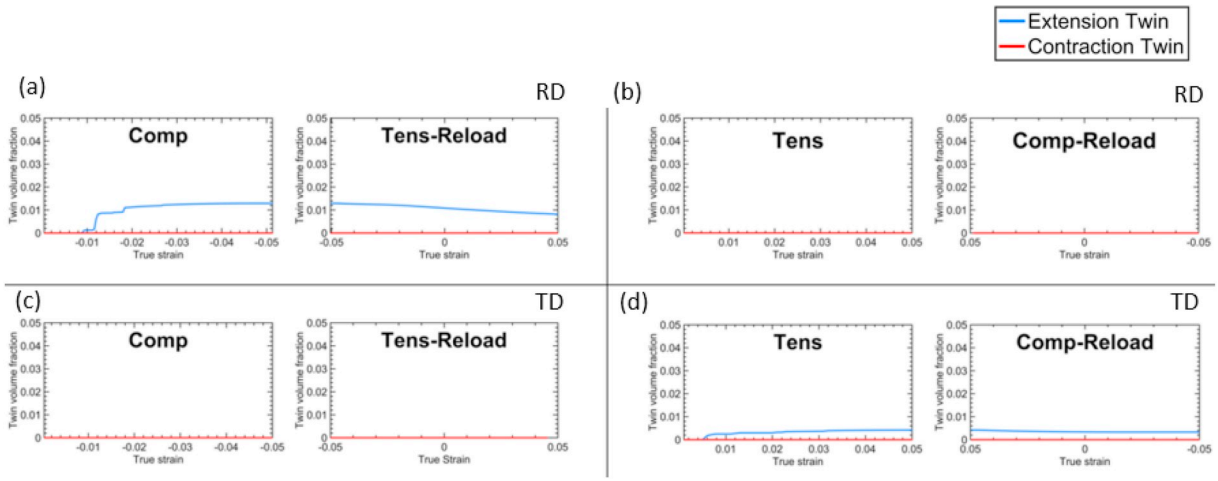

Fig. 11. Calculated twin volume fraction of the mode without taking into account backstress development during the 5% cyclic loading test in RD and TD directions: (a)RD-CT; (b)RD-TC; (c)TD-CT; (d)TD-TC.

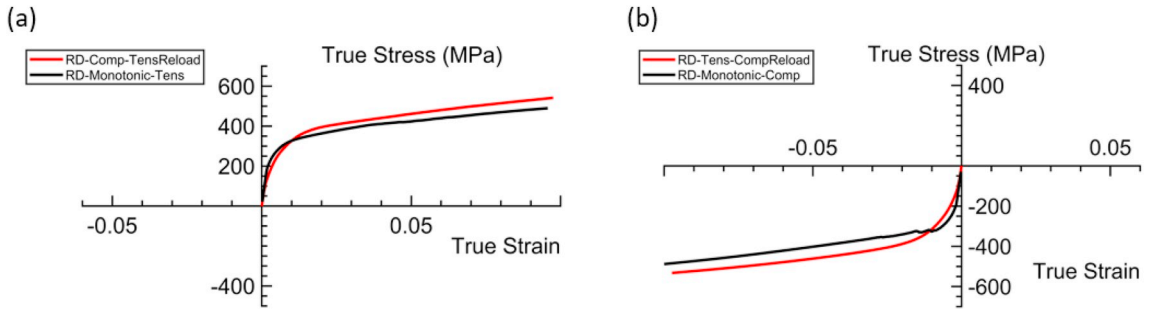

Fig. 12. (a) Comparison between monotonic tension in the RD direction and with the tension response following 5% compression in the RD direction and (b) Comparison between monotonic compression in the RD direction and with the compression response following 5% tension in the RD direction.

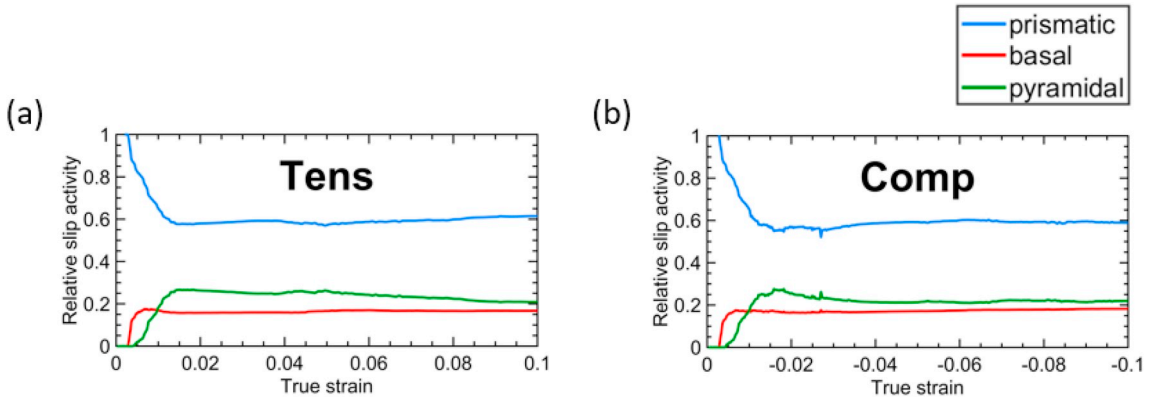

Fig. 13. Calculated slip activities during (a) monotonic tension and (b) monotonic compression in the RD direction.

backstress evolution during the deformation. While prismatic slip was dominant in all strain paths, the deformation was accommodated by multiple slip systems, wherein the relative amounts of basal slip and pyramidal slip were non-negligible. We find that the relative amounts of slip contributing to polycrystal level deformation did not substantially change with cyclic loading or sense of loading, provided the loading direction was the same. The analysis indicates that type III, intra-granular backstresses develop more strongly in $\langle c + a \rangle$ pyramidal slip than the other two $\langle a \rangle$ type slip modes. As a result, pyramidal slip backstresses that develop in

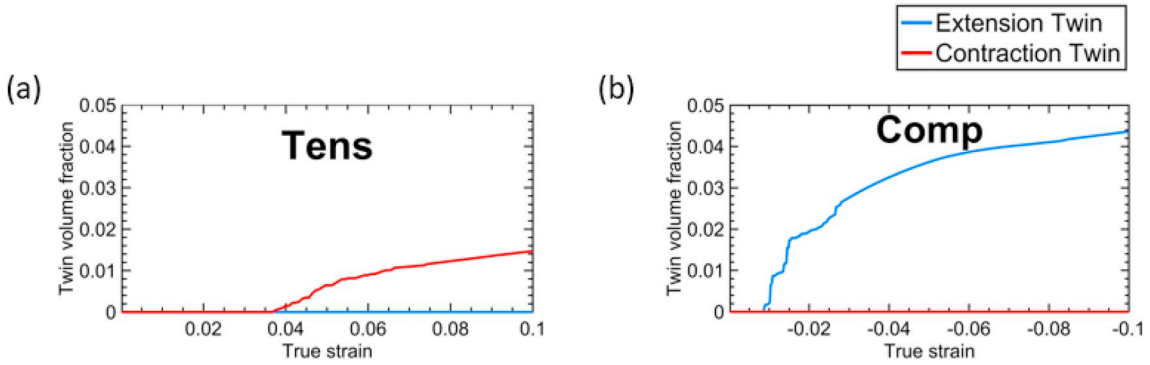

Fig. 14. Calculated twin volume fraction evolution with straining in (a) monotonic tension and (b) monotonic compression in the RD direction.

forward loading make deformation twinning by both extension and contraction modes more favorable. In reverse loading, pyramidal slip is favored over twinning due to the reversion of the sign of the backstresses. Consequently, the material develops more twins when strained from an undeformed state than when strained after pre-straining in the opposing direction.

Declaration of competing interest

The authors declare that they have no known competing financial interests or personal relationships that could have appeared to influence the work reported in this paper.

Acknowledgments

The authors gratefully acknowledge support from the U.S. National Science Foundation (NSF) under grant no. CMMI-1728224 (UCSB) and CMMI-1727495 (UNH).

Appendix

The Cauchy stress $\boldsymbol{\sigma}$ is determined by integrating the stress rate in Eqs. A.1 - A.5 from t to $t + \Delta t$, which gives:

$$\int_t^{t+\Delta t} \dot{\boldsymbol{\sigma}} dt = \int_t^{t+\Delta t} \frac{d\boldsymbol{\sigma}}{dt} dt = \boldsymbol{\sigma}_{t+\Delta t} - \boldsymbol{\sigma}_t \tag{A.1}$$

$$\boldsymbol{\sigma}_{t+\Delta t} = \boldsymbol{\sigma}_t + \int_t^{t+\Delta t} \dot{\boldsymbol{\sigma}} dt \tag{A.2}$$

The integration is performed explicitly. First, each time increment Δt is divided into n sub-steps, denoted with $i = 1, \ldots, n$. The stress in the ith sub-step σ_i is, therefore, expressed as

$$\dot{\boldsymbol{\sigma}}_i = \frac{\boldsymbol{\sigma}_{i+1} - \boldsymbol{\sigma}_i}{\frac{\Delta t}{n}} \tag{A.3}$$

Letting $\varepsilon_i = \frac{\Delta \varepsilon}{\Delta t}$ be the strain rate in the sub-step, we rewrite Eq. 3

$$\boldsymbol{\sigma}_{i+1} = \boldsymbol{\sigma}_i + \frac{\Delta t}{n} \mathbf{L}_i \dot{\boldsymbol{\varepsilon}}_i + \frac{\Delta t}{n} (< \mathbf{W}_i^c \boldsymbol{\sigma}_i^c > - < \boldsymbol{\sigma}_i^c \mathbf{W}_i^c >) \tag{A.4}$$

Finally the Cauchy stress $\boldsymbol{\sigma}_{t+\Delta t}$ at the end of the time increment Δt is

$$\boldsymbol{\sigma}_{t+\Delta t} = \boldsymbol{\sigma}_t + \sum_{i=1}^{n} \mathbf{L}_i \frac{\Delta \varepsilon}{n} + \frac{1}{n} \sum_{i=1}^{n} (< \mathbf{W}_i^c \Delta t \boldsymbol{\sigma}_i^c > + < \mathbf{W}_i^c \Delta t \boldsymbol{\sigma}_i^c)^T >) \tag{A.5}$$

where $\Delta \varepsilon$ is the increment in strain. The number of sub-steps, n, is determined by the following condition: $\max(\Delta \varepsilon_{ij}/n) \leq \kappa$, where κ is the threshold value on the order of $1 \times 10^{-0.4}$. These increments tend to be smaller during the elastic-plastic transition than in the plastic region.

References

Ardeljan, M., Knezevic, M., Nizolek, T., Beyerlein, I.J., Mara, N.A., Pollock, T.M., 2015. A study of microstructure-driven strain localizations in two-phase polycrystalline HCP/BCC composites using a multi-scale model. Int. J. Plast 74, 35–57.

Ardeljan, M., Savage, D.J., Kumar, A., Beyerlein, I.J., Knezevic, M., 2016. The plasticity of highly oriented nano-layered Zr/Nb composites. Acta Mater. 115, 189–203.

Bauschinger, J., 1886. Über die Veränderung der Elasticitätsgrenze und Festigkeit des Eisen und Stahls durch Strecken und Quetschen, durch Erwarmen und Abkühlen und durch oftmal wiederholte Beanspruchung. Mitteilungen aus dem mechanisch-technischen Laboratorium der k polytechnischen Schule, 1877–1836.

Bate, P.S., Wilson, D.V., 1986. Analysis of the bauschinger effect. Acta Metall. 34, 1097–1105.

Becker, H., Pantleon, W., 2013. Work-hardening stages and deformation mechanism maps during tensile deformation of commercially pure titanium. Comput. Mater. Sci. 76, 52–59.

Benmhenni, N., Bouvier, S., Brenner, R., Chauveau, T., Bacroix, B., 2013. Micromechanical modelling of monotonic loading of CP -Ti: correlation between macroscopic and microscopic behaviour. Mater. Sci. Eng. A 573, 222–233.

Beyerlein, I.J., Kumar, M.A., 2019. In: Andreoni, Wanda, Yip, Sidney (Eds.), The Stochastic Nature of Deformation Twinning: Application to HCP Metals" Handbook of Materials Modeling: Volume 2 Applications: Current and Emerging Materials. Springer Nature (in press).

Beyerlein, I.J., Zhang, X., Misra, A., 2014. Growth twins and deformation twins in metals. Annu. Rev. Mater. Res. 44, 329–363.

Beyerlein, I.J., Tomé, C.N., 2008. A dislocation-based constitutive law for pure Zr including temperature effects. Int. J. Plast 24, 867–895.

Buckley, S.N., Entwistle, K.M., 1956. The bauschinger effect in super-pure aluminum single crystals polycrystals. Acta Metall. 4, 352–361.

Britton, T.B., Dunne, F.P.E., Wilkinson, A.J., 2015. On the mechanistic basis of deformation at the microscale in hexagonal close-packed metals. Proc. R. Soc. A: Math. Phys. Eng. Sci. 471, 1–29.

Chichili, D.R., Ramesh, K.T., Hemker, K.J., 1998. The high-strain-rate response of alpha-titanium: experiments, deformation mechanisms and modeling. Acta Mater. 46, 1025–1104.

Conrad, H., 1981. Effect of interstitial solutes on the strength and ductility of titanium. Prog. Mater. Sci. 26, 123–403.

Demir, E., Raabe, D., 2010. Mechanical and microstructural single-crystal Bauschinger effects: observation of reversible plasticity in copper during bending. Acta Mater. 58, 6055–6063.

Eshelby, J.D., 1957. The determination of the elastic field of an ellipsoidal inclusion, and related problems. Proc. R. Soc. Lond. A 241, 376–396.

Ghorbanpour, S., Zecevic, M., Kumar, A., Jahedi, M., Bicknell, J., Jorgensen, L., et al., 2017. A crystal plasticity model incorporating the effects of precipitates in superalloys: application to tensile, compressive, and cyclic deformation of inconel. Int. J. Plast 718, 162–185.

Gloaguen, D., Oum, G., Legrand, V., Fajoui, J., Branchu, S., 2013. Experimental and theoretical studies of intergranular strain in an alpha titanium alloy during plastic deformation. Acta Mater. 61, 5779–5790.

Gurao, N.P., Kapoor, R., Suwas, S., 2011. Deformation behaviour of commercially pure titanium at extreme strain rates. Acta Mater. 59, 3431–3446.

Hama, T., Kariyazaki, Y., Hosokawa, N., Fujimoto, H., Takuda, H., 2012. Work-hardening behaviors of magnesium alloy sheet during in-plane cyclic loading. Mater. Sci. Eng. A 551, 209–217.

Hama, T., Kobuki1, A., Fujimoto, H., Takuda, H., 2016. Crystal-plasticity finite-element analysis of deformation behavior in a commercially pure titanium sheet. J. Phys. 734.

Hama, T., Nagao, H., Kobuki, A., Fujimoto, H., Takuda, H., 2015. Work-hardening and twinning behaviors in a commercially pure titanium sheet under various loading paths. Mater. Sci. Eng. A 620, 390–398.

Han, W.Z., Carpenter, J.S., Wang, J., Beyerlein, I.J., Mara, N.A., 2012. Atomic-level study of twin nucleation from fcc/bcc interfaces in nanolamellar composites. Appl. Phys. Lett. 100, 011911.

Hosford, W.F., 1993. The Mechanics of Crystals and Textured Polycrystals. Oxford University Press, New York,, pp. 163–184.

Hasegawa, T., Yakou, T., Karashima, S., 1975. Deformation behaviour and dislocation structures upon stress reversal in polycrystalline aluminium. Mater. Sci. Eng. 20,267–276.

Hutchinson, J., 1970. Elastic-plastic behaviour of polycrystalline metals and composites. Proc. R. Soc. Lond. A. Math. Phys. Sci. 319, 247–272.

Kassner, M.E., Geantil, P., Levine, L.E., 2013. Long range internal stresses in single-phase crystalline materials. Int. J. Plast. 45, 44–60.

Kalidindi, S.R., Duvvuru, H.K., Knezevic, M., 2006. Spectral calibration of crystal plasticity models. Acta Mater. 54, 1795–1804.

Kitayama, K., Tomé, C.N., Rauch, E.F., Gracio, J.J., Barlat, F., 2013. A crystallographic dislocation model for describing hardening of polycrystals during strain path changes. Application to low carbon steels. Int. J. Plast. 46, 54–69.

Knezevic, M., Beyerlein, I.J., Brown, D.W., Sisneros, T.A., Tomé, C.N., 2013. A polycrystal plasticity model for predicting mechanical response and texture evolution during strain-path changes: application to Beryllium. Int. J. Plast. 49, 185–198.

Knezevic, M., Lebensohn, R.A., Cazacu, O., Revil-Baudard, B., Proust, G., Vogel, S.C., Nixon, M.E., 2013. Modeling bending of α-titanium with embedded polycrystal plasticity in implicit finite elements. Mater. Sci. A 564, 116–126.

Knezevic, M., Drach, B., Ardeljan, M., Beyerlein, I.J., 2014. Three dimensional predictions of grain scale plasticity and grain boundaries using crystal plasticity finite element models. Comput. Methods Appl. Mech. Eng. 277, 239–259.

Knezevic, M., Zecevic, M., Beyerlein, I.J., Bingert, J.F., McCabe, R.J., 2015. Strain rate and temperature effects on the selection of primary and secondary slip and twinning systems in HCP Zr. Acta Mater. 88, 55–73.

Knezevic, M., Lebensohn, R.A., Cazacu, O., Revil-Baudard, B., Proust, G., Vogel, S.C., Nixon, M.E., 2013. Modeling bending of α-titanium with embedded polycrystal plasticity in implicit finite elements. Mater. Sci. Eng. A 564, 116–126.

Kumar, M.A., Beyerlein, I.J., Lebensohn, R.A., Tomé, C.N., 2017. Modeling the effect of neighboring grains on twin growth in HCP polycrystals. Model. Simul. Mater. Sci. Eng. 25, 064007.

Kumar, M.A., Morrow, B., McCabe, R.J., Beyerlein, I.J., 2017. An atomic-scale modeling and experimental study of $< c + a >$ dislocations in Mg. Mater. Sci. Eng. A 695, 270–278.

Lebensohn, R.A., Tomé, C.N., 1993. A self-consistent anisotropic approach for the simulation of plastic deformation and texture development of polycrystals: application to zirconium alloys. Acta Metall. Mater. 41, 2611–2624.

Lebensohn, R.A., Kanjarla, A.K., Eisenlohr, P., 2012. An elasto-viscoplastic formulation based on fast Fourier transforms for the prediction of micromechanical fields in polycrystalline materials. Int. J. Plast. 32–33, 59–69.

Lentz, M., Behringer, A., Fahrenson, C., Beyerlein, I.J., Reimers, W., 2014. Grain size effects on primary, secondary and tertiary twin development in Mg-4wt%Li(-1wt %Al) alloys. Metall. Mater. Trans. A 45, 4737–4741.

Lentz, M., Klaus, M., Beyerlein, I.J., Zecevic, M., Reimers, W., Knezevic, M., 2015. In-situ X-ray diffraction and crystal plasticity modeling of the deformation behavior of extruded Mg-Li-(Al) alloys: an uncommon tension-compression asymmetry. Acta Mater. 86, 254–268.

Lorentzen, T., Daymond, M.R., Clausen, B., Tomé, C.N., 2002. Lattice strain evolution during cyclic loading of stainless steel. Acta Mater 50, 1627–1638.

Ma, C., Wang, H., Hama, T., Guo, X., Mao, X., Wang, J., Wu, P., 2019. Twinning and detwinning behaviors of commercially pure titanium sheets. Int. J. Plast. 121.

Mughrabi, H., 1983. Dislocation wall and cell structures and long-range internal stresses in deformed metal crystals. Acta Metall. 31, 1367–1379.

Mullins, S., Patchett, B.M., 1981. Deformation microstructures in titanium sheet metal. Metall.Trans. A 12, 853–863.

Niezgoda, S.R., Kanjarla, A.K., Beyerlein, I.J., Tomé, C.N., 2014. Stochastic modeling of twin nucleation in polycrystals: an application in hexagonal close-packed metals. Int. J. Plast. 56, 119–138.

Nieh, T.G., Nix, W.D., 1986. Unloading yield effects in aluminum alloys. Metall. Metall. Trans. A 17, 121–126.

Orowan, E., 1959. In: Rassweiler, G.M., Grube, W.L. (Eds.), Causes and Effects of Internal Stresses, General Motors Symposium. Elsevier, Amsterdam, pp. 59–80.

Paton, N.E., Backofen, W., 1970. Plastic deformation of titanium at elevated temperatures. Metall. Trans. 1, 2839–2847.

Peng, J., Zhou, C.Y., Dai, Q., He, X.H., Yu, X., 2014. Fatigue and ratcheting behaviors of CP-Ti at room temperature. Mater. Sci. Eng. A 590, 329–337.

Risse, M., Lentz, M., Fahrenson, C., Reimers, W., Knezevic, M., Beyerlein, I.J., 2017. Temperature and loading direction dependent deformation behavior of an extruded Mg-4wt%Li alloy: experiments and polycrystal modeling. Metall. Mater. Trans. A 48, 446–458.
Sauzay, M., 2008. Analytical modelling of intragranular backstresses due to deformation induced dislocation microstructures. Int. J. Plast. 24, 727–745.
Shamsaei, N., Gladskyi, M., Panasovskyi, K., Shukaev, S., Fatemi, A., 2010. Multiaxial fatigue of titanium including step loading and load path alteration and sequence effects. Int. J. Fatigue 32, 1862–1874.
Seeger, A., 1957. Glide and work hardening in face-centered cubic and hexagonal close-packed metals. In: Fisher, J.C. (Ed.), Dslocations and Mechanical Properties of Cryslals. Wiley, New York, p. 243.
Sinha, S., Ghosh, A., Gurao, N.P., 2016. Effect of initial orientation on the tensile properties of commercially pure titanium. Philos. Mag. 96, 1485–1508.
Simmons, G., Wang, H., 1971. Single Crystal Elastic Constants and Calculated Aggregate Properties, second ed.
Suwas, S., Beausir, B., Tóth, L.S., Fundenberger, J.-J., Gottstein, G., 2011. Texture evolution in commercially pure titanium after warm equal channel angular extrusion. Acta Mater. 59, 1121–1133.
Stanford, N., Carlson, U., Barnett, M.R., 2008. Deformation twinning and the Hall–Petch relation in commercial purity Ti. Metall. Mater. Trans. A 39, 934–944.
Stout, M., Rollett, A., 1990. Large-strain Bauschinger effects in fcc metals and alloys. Metall. Mater. Trans. A 21, 3201–3213.
Tirry, W., Bouvier, S., Benmhenni, N., Hammami, W., Habraken, A.M., Coghe, F., Schryvers, D., Rabet, L., 2012. Twinning in pure Ti subjected to monotonic simple shear deformation. Mater. Char. 72, 24–36.
Turner, P.A., Tomé, C.N., 1994. A study of residual stresses in Zircaloy-2 with rod texture. Acta Metall. Mater. 42, 4143–4153.
Tritschler, M., Butz, A., Helm, D., Falkinger, G., Kiese, J., 2014. Experimental analysis and modeling of the anisotropic response of titanium alloy Ti-X for quasi-static loading at room temperature. Int. J. Material Form. 7, 259–273.
Wang, H., Wu, P.D., Wang, J., 2013. Modeling inelastic behavior of magnesium alloys during cyclic loading–unloading. Int. J. Plast. 47, 49–64.
Wang, H., Wu, P.D., Wang, J., Tomé, C.N., 2013. A crystal plasticity model for hexagonal close packed (HCP) crystals including twinning and detwinning mechanisms. Int. J. Plast. 49, 36–52.
Wang, L., Zheng, Z., Phukan, H., Kenesei, P., Park, J.-S., Lind, J., Suter, R.M., Bieler, T.R., 2017. Direct measurement of critical resolved shear stress of prismatic and basal slip in polycrystalline Ti using high energy X-ray diffraction microscopy. Acta Mater. 132, 598–610.
Warwick, J.L.W., Jones, N.G., Rahman, K.M., Dye, D., 2012. Lattice strain evolution during tensile and compressive loading of CP Ti. Acta Mater. 60, 6720–6731.
Wen, W., Borodachenkova, M., Tomé, C.N., Vincze, G., Rauch, E.F., Barlat, F., Gracio, J.J., 2014. Mechanical behavior of Mg subjected to strain path changes: experiments and modeling. Int. J. Plast. 73, 171–183.
Weng, G.J., 1980. Constitutive equations of single crystals and polycrystalline aggregates under cyclic loading. Int. J. Eng. Sci. 18, 1385–1397.
Weng, G.J., 1979. Kinematic hardening rule in single crystals. Int. J. Solids Struct. 15, 861–870.
Wilson, D.V., Zandrahimi, M., Roberts, W.T., 1990. Effects of changes in strain path on work-hardening in CP aluminium and an Al–Cu–Mg alloy. Acta Metall. Mater. 38, 215–226.
Wollmershauser, J.A., Clausen, B., Agnew, S.R., 2012. A slip system-based kinematic hardening model application to in situ neutron diffraction of cyclic deformation of austenitic stainless steel. Int. J. Fatigue 36, 181–193.
Won, J., Choi, S., Yeom, J., Hyun, Y., Lee, C.S., Park, S.H., 2017. Anisotropic twinning and slip behaviors and their relative activities in rolled alpha-phase titanium. Mater. Sci. Eng. A 698, 54–62.
Won, J.W., Park, C.H., Hong, S.G., Lee, C.S., 2015. Deformation anisotropy and associated mechanisms in rolling textured high purity titanium. J. Alloy. Comp. 651, 245–254.
Wronski, M., Kumar, M.A., Capolungo, L., McCabe, R.J., Wierzbanowski, K., Tomé, C.N., 2018. Deformation behavior of CP-titanium: experiment and crystal plasticity modeling. Mater. Sci. Eng. A 724, 289–297.
Wu, X., Kalidindi, S.R., Necker, C., Salm, A.A., 2008. Modeling anisotropic stress-strain response and crystallographic texture evolution in α-titanium during large plastic deformation using taylor-type models:influence of initial texture and purity. Metall. Mater. Trans. A 39, 3046–3054.
Xu, F., Zhang, X., Ni, H., Liu, Q., 2012. $\{11\bar{2}4\}$ deformation twinning in pure Ti during dynamic plastic deformation. Mater. Sci. A 541, 190–195.
Yapici, G.G., Karaman, I., Luo, Z.P., 2006. Mechanical twinning and texture evolution in severely deformed Ti–6Al–4V at high temperatures. Acta Mater. 54, 3755–3771.
Yoo, M.H., Loh, B.T.M., 1970. Structural and elastic properties of zonal twin dislocations in anisotropic crystals. In: Simmons, J.A., De Wit, R., Bullough, R. (Eds.), Fundamental Aspects of Dislocation Theory. Nat. Bur. Stand. (US) Special Publication 317, vol. 1, pp. 479–493.
Zang, S.-l, Lee, M.-g, HoonKim, J., 2013. Evaluating the significance of hardening behavior and unloading modulus under strain reversal in sheet springback prediction. Int. J. Mech. Sci. 77, 194–204.
Zecevic, M., Knezevic, M., 2015. A dislocation density based elasto-plastic self-consistent model for the prediction of cyclic deformation: application to AA6022-T4. Int. J. Plast. 72, 200–217.
Zecevic, M., McCabe, R.J., Knezevic, M., 2015. A new implementation of the spectral crystal plasticity framework in implicit finite elements. Mech. Mater. 84, 114–126.
Zecevic, M., Korkolis, Y.P., Kuwabara, T., Knezevic, M., 2016. Dual-phase steel sheets under cyclic tension–compression to large strains: experiments and crystal plasticity modeling. J. Mech. Phys. Solids 96, 65–87.
Zecevic, M., Knezevic, M., 2018. Latent hardening within the elasto-plastic self-consistent polycrystal homogenization to enable the prediction of anisotropy of AA6022-T4 sheets. Int. J. Plast. 105, 141–163.
Zhang, D., Jiang, L., Wang, X., Beyerlein, I.J., Minor, A., Schoenung, J., Mahajan, S., Lavernia, E., 2019. In-situ transmission electron microscopy investigation on <c+a> slip in Mg. J. Mater. Res. 34, 1499–1508.
Zheng, S.J., Wang, J., Carpenter, J.S., Mook, W., Dickerson, P., Mara, N.A., Beyerlein, I.J., 2014. Plastic instability mechanisms in bimetallic nanolayered composites. Acta Mater. 79, 282–291.